LBNL-55855

ERNEST ORLANDO LAWRENCE
BERKELEY NATIONAL LABORATORY

Recombination and Propagation of Quasiparticles in Cuprate Superconductors

N. Gedik

Materials Sciences Division

May 2004

Ph.D. Thesis

LBNL-55855

Recombination and Propagation of Quasiparticles in Cuprate Superconductors

Nuh Gedik
Ph.D. Thesis

Department of Physics
University of California, Berkeley

and

Materials Sciences Division
Ernest Orlando Lawrence Berkeley National Laboratory
University of California
Berkeley, CA 94720

May 2004

This work was supported by the Director, Office of Science, of the U.S. Department of Energy under Contract No. DE-AC03-76SF00098.

DISCLAIMER

Abstract

Recombination and Propagation of Quasiparticles in Cuprate Superconductors

by

Nuh GEDIK

Doctor of Philosophy in Physics

University of California at Berkeley

Professor Joseph Orenstein, Chair

Rapid developments in time-resolved optical spectroscopy have led to renewed interest in the nonequilibrium state of superconductors and other highly correlated electron materials. In these experiments, the nonequilibrium state is prepared by the absorption of short (less than 100 fs) laser pulses, typically in the near-infrared, that perturb the density and energy distribution of quasiparticles. The evolution of the nonequilibrium state is probed by time-resolving the changes in the optical response functions of the medium that take place after photoexcitation. Ultimately, the goal of such experiments is to understand not only the nonequilibrium state, but to shed light on the still poorly understood equilibrium properties of these materials.

We report nonequilibrium experiments that have revealed aspects of the cuprates that have been inaccessible by other techniques. Namely, the diffusion and recombination coefficients of quasiparticles have been measured in both $YBa_2Cu_3O_{6.5}$ and $Bi_2Sr_2CaCu_2O_{8+x}$

using time-resolved optical spectroscopy. Dependence of these measurements on doping, temperature and laser intensity is also obtained.

To study the recombination of quasiparticles, we measure the change in reflectivity ΔR which is directly proportional to the nonequilibrium quasiparticle density created by the laser. From the intensity dependence, we estimate β, the inelastic scattering coefficient and γ_{th} thermal equilibrium quasiparticle decay rate. We also present the dependence of recombination measurements on doping in $Bi_2Sr_2CaCu_2O_{8+x}$. Going from underdoped to overdoped regime, the sign of ΔR changes from positive to negative right at the optimal doping. This is accompanied by a change in dynamics. The decay of ΔR stops being intensity dependent exactly at the optimal doping. We provide possible interpretations of these two observations.

To study the propagation of quasiparticles, we interfered two laser pulses to introduce a spatially periodic density of quasiparticles. Probing the evolution of the initial density through space and time yielded the quasiparticle diffusion coefficient, and both inelastic and elastic scattering rates. Measured diffusion coefficient suggests that the quasiparticles induced by the laser occupy primarily states near the antinodal regions of the Brillouin zone.

Professor Joseph Orenstein
Dissertation Committee Chair

To everyone who supported me

Contents

List of Figures

Acknowledgements

The help and support of many people were crucial for my achievements in the graduate school. I have received support in many forms from a number of people who ultimately made the experience what it was.

I was very lucky to have Joe Orenstein as my research advisor. He is an excellent mentor with guidance and support as well as a perfect teacher with a unique way of scientific thinking. Gino Segre is my patient trainer in the lab. Beyond teaching me in the lab, he provided the basic experimental setup as the starting point for my experiment. John Corson and Steve Dodge also provided me support in the lab. Chris Weber is a friend beyond being a co-worker. Chris Weber and Matt Langner are successors in the lab who will carry this work forward. Marc Carnahan and Chih Wei Lai are companions that provided support and expertise in various forms. Doug Bonn's group and Yoich Ando's group are world-class specialists in sample growing without whom our research would not be possible. Dung-hai Lee and Joel Moore provided expertise in theory for our experiments. Anne Takizawa made the administrative work very easy.

Although they were far away, my family provided me support throughout my study. My roommates and friends outside the school became my local family and helped me throughout my five years in Berkeley. They provided a warm support and a shelter from physics.

Thanks to all of you.

Chapter 1

Introduction

As we approach the end of second decade since the discovery of high temperature superconductivity, the mechanism remains to be a mystery. In particular, we still don't know the nature of the bosonic excitation that binds the electrons together to form a cooper pair in these materials. Studying the low energy excitations is one approach in search for this mysterious boson.

One complication that cuprates have compared to conventional superconductors is that the superconducting gap is not uniform across the fermi surface. It has d-wave symmetry compared to s-wave symmetry in conventional superconductors. The gap vanishes in 4 directions (nodal points) 45^0 to the Cu-O bonds, and it has the maximum value along the Cu-O bonds (antinodal points). Therefore one can get two types of excitations in the vicinity of these two points, namely nodal and antinodal excitations. Since the typical maximum value of the gap is on the order of 50 meV, in thermal equilibrium only nodal quasiparticles would be present in the superconducting state. And in fact, all the

experiments done in thermal equilibrium probes the properties of nodal quasiparticles since the number of antinodal quasiparticles is exponentially smaller than the nodal ones in thermal equilibrium. On the other hand, since the antinodal quasiparticles are the ones that experience the pairing interaction most strongly, their properties would be far more interesting and useful to understand the nature of pairing. In this thesis, we argue that non-equilibrium experiments are ideal ways of creating and probing antinodal quasiparticles.

In these experiments, the nonequilibrium state is prepared by the absorption of short (less than 100 fs) laser pulses, typically in the near-infrared, that perturb the density and energy distribution of quasiparticles. The evolution of the nonequilibrium state is probed by time-resolving the changes in the optical response functions of the medium that take place after photoexcitation. The nonequilibrium state of the cuprate superconductors, in particular, has been studied extensively. Ultimately, the goal of such experiments is to understand not only the nonequilibrium state, but to shed light on the still poorly understood equilibrium properties of these materials. Recently, nonequilibrium experiments have revealed aspects of the cuprates that have been inaccessible by other techniques. For example, both the diffusion and recombination coefficients of antinodal quasiparticles have been measured in underdoped single crystals of $YBa_2Cu_3O_{6.5}$ using time-resolved optical spectroscopy.

This thesis is organized as follows: In Chapter 2, we describe the pump probe spectroscopy, the experimental technique used to measure the recombination of quasiparticles. Chapter 3 describes the results of pump probe experiments done on $YBa_2Cu_3O_{6.5}$ and their implications . In Chapter 4, we study the pump probe signal as a function of doping in the

$Bi_2Sr_2CaCu_2O_{8+d}$ system. In Chapter 5, transient grating spectroscopy, the experimental technique used to measure the diffusion of quasiparticles is described. Chapter 6 presents the first measurement of quasiparticle diffusion and its implications. Below we provide a brief summary of each chapter.

In Chapter 2, we begin by introducing pump probe spectroscopy. We explain our experimental setup in detail, and describe how we can measure very small changes in reflectivity. Having this very high sensitivity of 10^{-7} in fractional reflectivity change ($\Delta R/R$) was very crucial for our experiments.

In Chapter 3, we report results and analysis of time-resolved photoinduced reflectivity experiments on the cuprate superconductor $YBa_2Cu_3O_{6.5}$. The sample, which has T_c=45 K, was characterized by a high degree of purity and Ortho II ordering. The change in reflectivity ΔR was induced and probed using pulses of 100 femtosecond duration and photon energy 1.55 eV from a Ti:Sapphire laser. We provide a detailed picture of the decay rate γ of ΔR as a function of temperature T and pump intensity I. At low T, γ decreases linearly with decreasing I, extrapolating to nearly zero in the limit that I tends to zero. At higher temperature γ has the same linear dependence, but with nonzero limit as $I \rightarrow 0$. In the interpretation of these results we assume that ΔR is proportional to the nonequilibrium quasiparticle density created by the laser. From an analysis of the γ vs. I we estimate β, the coefficient of proportionality relating the quasiparticle decay rate to the density. The intercept of γ vs. I yields the thermal equilibrium quasiparticle decay rate. In a discussion section, we argue that the quasiparticles induced by the laser occupy primarily states near the antinodal regions of the Brillouin zone. We explain the divergence of the lifetime of these

particles as T and I both tend to zero as a consequence of momentum and energy conservation in electron-electron scattering. Next, we discuss the significance of the measured value of β, which is ≈ 0.1 cm^{2}s^{-1}. We point out that the natural unit for β in a two-dimensional superconductor is $\hbar/m^*$, and define a dimensionless constant C such that $\beta \equiv C\hbar/m^*$. If the decay process is one in which quasiparticles return to the condensate with emission of a phonon, then C is a measure of the electron-phonon interaction. Alternatively, expressing the marginal Fermi liquid scattering in the normal state in terms of an effective β implies $C = 1/\pi$, which is in excellent agreement with the experimentally determined value in the superconducting state.

In Chapter 4, we study the pump probe signal as a function of laser intensity and carrier concentration in $Bi_2Sr_2CaCu_2O_{8+d}$. We find that there is an abrupt change in the ΔR at optimal doping. In the underdoped side of the diagram ΔR is positive and the decay rate γ is linear in intensity. On the overdoped side, ΔR becomes negative and the decay is essentially independent of intensity. We discuss the potential meaning of these two important observations.

In Chapter 5, we describe transient grating spectroscopy. We describe our heterodyne detected transient reflecting grating setup. Use of a custom made diffractive optics together with a novel way of in situ phase calibration is described.

In Chapter 6, we describe the first measurements of diffusion constant of nonequilibrium quasiparticles in cuprates. The measured diffusion constant turns out to be 2 order of magnitude smaller than the diffusion constant of nodal quasiparticles estimated from microwave experiments done in thermal equilibrium. This is presented as a direct evidence

that non-equilibrium experiments are creating and probing antinodal quasiparticles. Mean free path and elastic scattering rate is estimated using the measured diffusion constant. We discuss the implication of obtained mean free path on the electronic inhomogeneity seen by STM experiments on the $Bi_2Sr_2CaCu_2O_{8+d}$ system. Our results raise the possibility that the disparities in relaxation rate and sign of ΔR observed in other cuprate samples may be a consequence of a general, or perhaps universal, change in quasiparticle dynamics that takes place at optimal doping.

Chapter 2

Pump Probe Spectroscopy

Pump probe spectroscopy measures the transient change in reflectivity (ΔR) of a sample induced by an ultrashort laser pulse. ΔR is measured by using a weaker laser pulse. The first strong pulse which generates ΔR is called "pump" pulse, and the second weaker pulse that measures the change is called the "probe" pulse. By delaying the probe pulse with respect to the pump pulse in time, ΔR is obtained as a function of time ($\Delta R(t)$). Measuring $\Delta R(t)$ is a way of probing the time evolution of the nonequilibrium state created by the pump pulse.

This technique has been used successfully in a wide variety of applications. In superconductors, it can be used to study the quasiparticle dynamics. Quasiparticles are the elementary excitations of a superconductor, created when a Cooper pair of electrons breaks apart. In the experiment, an ultrafast laser pulse incident on the superconductor breaks apart the cooper pairs generating a nonequilibrium population of quasiparticles. Existence of nonequilibrium quasiparticles changes the equilibrium value of the reflectivity. As the

quasiparticles re-pair and join the condensate, reflectivity returns back to its equilibrium value. ΔR is proportional to the density of excess quasiparticles. Studying $\Delta R(t)$ as a function of experimental control parameters (i.e. temperature, laser intensity, polarization, magnetic field etc ...) yields information about quasiparticle dynamics. Typical fractional changes in reflectivity ($\Delta R/R$) are on the order of 10^{-4} - 10^{-5}. Our pump probe setup can measure $\Delta R/R$ as small as 10^{-7}.

2.1 Experimental Setup

In this section, I will describe the experimental setup in detail. Laser system and optics used in the experiment will be described in detail. Signal detection scheme and data analysis will also be discussed. Experimental improvements that contribute to the ultrahigh sensitivity will be explained.

2.1.1 Laser System and Optics

In figure 2.1 experimental setup is shown. Here we will describe the individual components of the setup in more detail.

The laser system used in the experiment has two parts. The first laser is a diode pumped Nd:Yag laser (Spectra Physics Millenia). It produces continuous wave output at 514 nm at a power of 4.5 Watts. This laser pumps a Ti:Sapphire laser (KM Labs). Ti:Saph laser converts the continuous wave pump laser into short laser pulses centered at 820 nm. These short pulses have a width of less than 100 fs and a repetition rate of 90 MHz. The average power is about 500 mW.

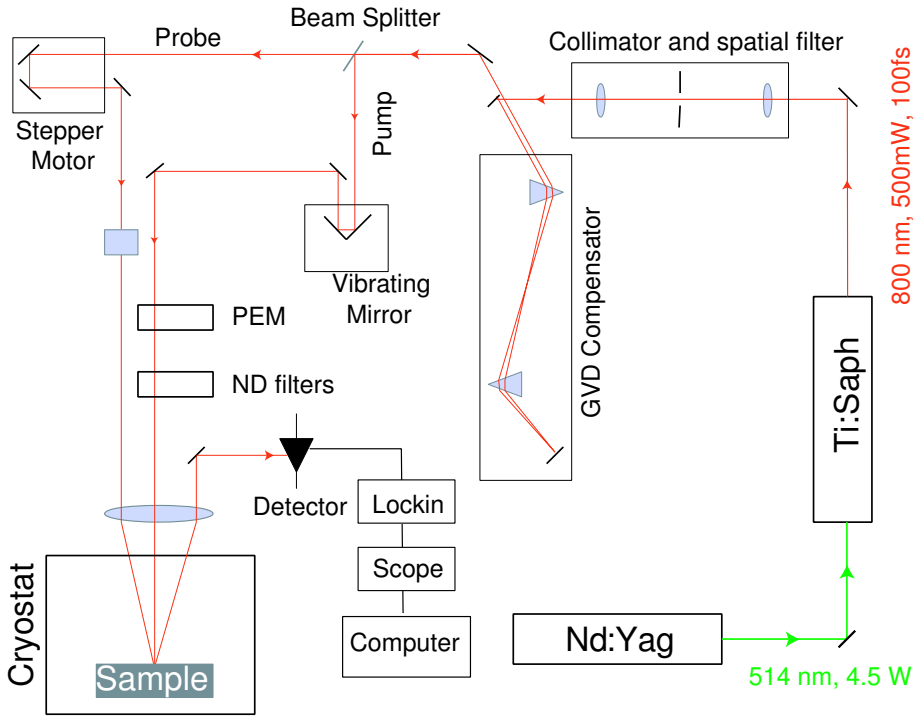

Figure 2.1: Optical Schematic of the apparatus. A discussion of the signal processing is included in the body.

After the laser there is a lens pair to collimate the beam. To minimize the divergence a pair of lens with equal focal lengths is used. The two lens are placed approximately twice the focal length ($2f$) away from each other. When the distance is exactly $2f$, the lens pair has no effect on divergence. One of the lens is mounted on a micrometer. By tuning the micrometer position, the divergence of the laser beam can be greatly improved. A 100 μm pinhole placed on the focal point between the lenses acts as a spatial filter. The spatial noise in the beam profile will focus on to a different point then the main beam. The pinhole is mounted on a XYZ stage. The power transmitted across the pinhole is maximized by optimizing the three micrometer axes. We obtain a very clean beam profile after the pinhole with more than 95% efficiency.

After the collimator, there is prism pair which compensates the group velocity dispersion (GVD). Since the laser has a limited pulse width in time, it has a finite bandwidth in frequency. The FWHM bandwidth in frequency is about 40 nm. Different frequency components that make up the pulse have different velocities inside the optics. Therefore the pulse will spread in time as it travels through the optics. This effect can be pre-compensated by using a prism pair. Prisms are placed at minimum deviation angle positions. The pair introduces a negative GVD that is proportional to the separation between the prisms. Also since the laser beam travels through the prisms, it introduces a positive GVD proportional to the amount of prism glass in the beam path. Each prism is mounted on a micrometer through which prisms can be inserted more into the beam or pulled away to change the amount of glass light travels. For both pump and probe arms, pulse width in time is minimized by fine tuning the prism separation and the micrometer positions. In our case, pump beam traveled through some more additional optics that was not in the probe beam's path (Photo elastic modulator and polarizer). So we have adjusted the prism pair causing the shortest pulse width at the sample position for the pump beam. Additional glass is placed on the probe arm to make the pulse with the same as the pump beam. Pulse with is measured by use of an external autocorrelator.

After the GVD compensator, there is a beam splitter which splits the laser beam into a stronger pump beam and a weaker probe beam. At this point, pump beam is about 10 times stronger than the probe beam. In the probe arm, there is a Klinger stepper motor which can change the beam path in steps of one micron. This stage is about 15 cm long, so it can generate a maximum of 1 ns time delay as the light travels back and forth. It is

only used when finding the zero time delay of the pump and the probe beams at the sample position. Once the position at which pump and probe pulses arrive at the sample at the same time is set, we do not use this stepper motor when taking data. In the actual data taking, the time delay is changed by a vibrating delay line (Clark-MXR ODL-150) placed in the pump arm. Frequency and the oscillation amplitude can be adjusted through the function generator which drives this instrument. Typical value for the frequency is 30 Hz and the delay amplitude can go up to 100 ps. Using a fast oscillating mirror to change the optical delay helps tremendously in terms of signal to noise compared to using a stepper motor.

Following the vibrating mirror in the pump arm, there is a photoelastic modulator (Hinds Instruments PEM-90). A PEM is an instrument used for modulating or varying the polarization of a beam of light at a fixed frequency. Its principle of operation is based on the photoelastic effect, in which a mechanically stressed sample exhibits birefringence proportional to the resulting strain. Typically, it contains a rectangular bar of suitable transparent material which is made to vibrate along one axis at its natural frequency by a quartz transducer. As the material vibrates, it generates a birefringence that also vibrates at the same frequency. In our case, the frequency of PEM is 50 kHz. We set the peak retardation amplitude in the controller to half the wavelength ($\lambda/2$).

Before the PEM, laser beam is polarized parallel to the optical table. The PEM is mounted such that its axis is at 45^0 to the incident polarization. Optical delay for the component of the light polarized along the PEM axis oscillates between 0 and $\lambda/2$. When the peak retardation is exactly $\lambda/2$, PEM acts like a half wave plate and it rotates

the polarization of light by 90^0. As the retardation of PEM oscillates between $\pm\lambda/2$, the polarization of light after PEM alters between unchanged, right circularly polarized, rotated by 90^0 and left circularly polarized states. After the PEM, there is a polarizer (not shown in figure 2.1) with its axis aligned perpendicular to the polarization of light before the PEM. When the retardation of PEM reaches $\lambda/2$, the laser beam after PEM is polarized along the polarizer axis and 100% goes through. When the retardation is 0, the laser beam is polarized perpendicular to the polarizer axis and it is blocked entirely. The intensity of light after the polarizer oscillates between full intensity and zero with twice the PEM frequency. Therefore, PEM combined with a polarizer acts like a chopper at 100 kHz. The controller for the PEM has an output at 100 kHz which we use as a reference signal for the lockin amplifier. The advantage of using a PEM rather than a simple chopper is the ability to chop at such a high frequency of 100 kHz. This greatly reduces the $1/f$ noise.

PEM and the polarizer are the optics that are only present in the pump arm. They introduce extra GVD compared to the probe arm. To compensate for this effect, we have placed a slab of quartz with appropriate thickness. To adjust the thickness, we first minimized the pulse width of the pump beam by adjusting the prism pairs. Then we monitored the probe pulse with and minimized it by placing an quartz slab with an appropriate thickness (shown as a glass rectangle in figure 2.1).

After the PEM and the polarizer, there is a set of neutral density (ND) filters placed on two computer controlled wheels (CVI lasers AB300 wheels) in the pump arm. They are used to change the intensity of the pump beam. Having the ND filters computer controlled is very convenient to study the intensity dependence of the signal. There is also

a similar set of manually controlled neutral density filters placed in the probe arm to adjust the probe intensity (not shown in the figure 2.1). Following the ND filters, half wave plates are used to rotate the polarization of the beams when studying the polarization dependence.

After this, there is a special lens (achromatic doublet with increased precision and minimum spherical aberration) used to focus the beams on to the sample. The focal length of the lens is 8 inches. Before the lens, the pump and the probe beams run parallel to each other along the lens axis separated from each other by half an inch. The beam diameter before the lens is about 2 mm. The focal spot size on the sample is 100 μm. To maximize the oveelap of the two beams, a pinhole mounted on a XYZ translational stage is used. First, pump beam is blocked and the focus of the probe beam is found by maximizing the power transmitted through the pinhole by optimizing the XYZ positions. Then, probe beam is blocked and pump light passing through the pinhole is maximized by adjusting the pump mirror before the lens.

Reflected probe from the sample is collected by a mirror and sent to a detector (we used a Nirvana Auto-Balanced photoreceiver in a single detector mode). Since we are trying to detect changes in the intensity of the probe beam due to modulation of the pump beam, any leakage of scattered pump light will generate noise at the detection frequency. To discriminate the pump scattering we cross-polarize pump and the probe beams, and use a polarizer before the detector aligned to pass the probe light and block the pump light.

2.1.2 Data Acquisition

The output of the detector is then sent to the lockin amplifier (Stanford Research Systems SR850) as the signal. A reference signal from the PEM's controller at 100 kHz

is used for the lockin reference. The output of the lockin is sent to a digital oscilloscope (Lecroy 9310M) and serves as the y-axis. As mentioned in the previous section, time delay between the pump and probe is varied by a vibrating delay line. A function generator drives the delay line via a driver module. The position of the delay line is converted to a voltage by the same delay line and sent to the oscilloscope. This signal serve as the x-axis. These two channels (x and y) are averaged by the oscilloscope and sent to the computer. Data acquisition software is written in LabWindowsCVI and Matlab is used to analyze the raw data.

To compromise between the signal to noise and the time resolution, time constant of the lockin is set to 30 μs. For this value of the time constant, time resolution is about 100 fs. This is plenty enough considering that we are studying decays with characteristic times of couple of picoseconds. When studying faster decays (i.e. at high temperatures or high intensities) a very simple modeling can be used to extract lifetimes on the order of couple hundred femtoseconds.

There are two basic modes that we operate the system. The most common way is to hold the temperature fixed and record the reflectivity traces as a function of time by sweeping the time delay. We change the pump intensity and record the time traces at different pump intensities at a fixed temperature. We then change the temperature to a different value to study the temperature dependence. The second mode of data taking is to fix the laser intensity and ramp up the temperature at a slow rate. We use the continuous averaging feature of the digital oscilloscope and record time traces and the temperature values at fixed time intervals. At the end we get a three dimensional data, where transient

reflectivity change is obtained as a continues function of temperature and time delay. The second method is used to get a quick overview of the general behavior of the signal, and first method is used for quantitative analysis.

2.2 Cryostats

We have used two different kinds of cryostats. In the earlier stages of the data taking, we were using a Janis 12CNDT magnet cryostat. It has a capability of applying magnetic field (up to 7 tesla) and cooling down to very low temperatures (down to 2 K). Because of the tedious cool down procedure and low angle of incidence capability of this system, we have switched to an Oxford Instruments Microstat. With this cryostat one can reach the base temperature of 4.2 K in about 2 hours starting from the room temperatures. Also since the sample is only about half an inch away from the window, we can obtain very large angle of incidence as required by the transient grating experiments (please see Chapter 5).

In both cases, the entire cryostat is mounted on a translation stage to facilitate fine positioning of the sample in the plane of the optical table. We can also set the pitch or height of the cryostat by adjusting its mount. This freedom is an indispensable feature of our apparatus, since the surface of the sample may not be reflecting the beam in a useful direction. We can also remedy situations in which certain parts of the sample may have too much pump scatter.

Knowing the exact temperature of the sample is crucial for understanding the temperature dependence of the signal. In both cryostats, there is a temperature sensor

mounted on the sample stick about an inch away from the sample. This distance has potential to cause error in temperature measurements due to thermal gradients. To remedy this, we have placed an additional temperature sensor (LakeShore CX-1050) to the back of the substrate. Samples and sensors are affixed with N type Apiezon cryogenic grease, or GE-7031 Varnish(LakeShore).

2.3 Experimental Improvements

In this section, we will describe the improvements made in the experimental setup. Through these improvements, we were able to measure fractional changes in reflectivity ($\Delta R/R$) of about $10^{-}7$. Having this kind of sensitivity made it possible to study the limit of very low intensity from which equilibrium properties of the sample can be deduced. Having a big dynamic range in intensity (three orders of magnitude) was crucial to understand the intensity dependence.

There are a number of factors that contribute to this ultrahigh sensitivity. First of all, chopping at a very high frequency of 100 kHz gets rid of most of the 1/f noise. Using a vibrating delay line rather than a stepper motor provides some additional averaging of the laser noise.

One of the major improvements that we did in the setup was to improve the collimation of the laser beams by introducing a lens pair. This turns out to be very important for the overlap of the pump and probe beams. If the beams are not properly collimated, the overlap of the beams at the sample position may occur at a different position than the focus of each beam where intensity is maximum. This would decrease the signal size. Optimizing

the collimation improved the overlap and the signal size.

The second improvement made to the setup is the automation of the neutral density filter wheels that control the intensity of the pump beam. When we are taking data, we fix the temperature and record time traces at different intensities. After placements of the automated nd filter wheels, we can program the computer to take a set of time traces at different intensities with different averaging times for each intensity. This way, we do not need to be in the lab to change intensity values after each scan. Since often the low intensity regime is of interest, studying the intensity dependence can take several hours.

Another improvement that is made to the setup is related to a low temperature problem that we encountered. One of the cryostats that we used (Oxford Instruments Microstat) is a cold finger cryostat. In this cryostat, the sample is mounted on a copper cold finger and is surrounded by vacuum. After cooling down to low temperature, the walls of the cryostat which are at room temperature begins to outgas. The molecules released from the room temperature walls stick and condense into cold places inside the cryostat. Since the sample is also at low temperature, sample surface is coated with this material slowly.

Reflectivity of the sample decreased to the third of its value after the cool down over the course of couple hours. Different samples showed different behaviors. For example, the reflectivity of the silicon did not change appreciably. This suggested that the problem is not caused by decrease in the sample surface quality. The reason for the change in reflectivity turns out to be impedance matching of the material (possibly water) condensing on to our sample. In impedance matching, a layer of film on a sample with a right index of

refraction and a certain thickness causes the reflectivity of the sample go to zero. Using a vacuum pump at low temperature did not significantly improve the situation. To solve this problem we introduced a thin coverslip between the room temperature windows and the sample. The coverslip attached to the cold finger is also at low temperature. Anything that comes out of the room temperature windows condenses into this cold window and does not change the reflectivity. This method completely solved the problem and provided a stable value of reflectivity for several hours.

Chapter 3

Recombination of quasiparticles

3.1 Introduction

A special property of the cuprate superconductors is that the energy required for the creation of a quasiparticle depends on the direction of its momentum [47]. The creation energy is zero for momenta in the 'nodal' direction, oriented at 45° relative to the Cu-O bond. The most energetically expensive quasiparticles are the 'antinodal' ones, whose momenta are nearly parallel to the bond. Because they feel the pairing interaction most strongly, their properties may hold the key to high-T_c superconductivity. Unfortunately, their tendency to form strong pairs makes them difficult to study. In thermal equilibrium the population of quasiparticles is overwhelmingly dominated by the low energy nodal ones. As a result, transport measurements performed in equilibrium, such as microwave [26] and thermal [53] conductivity, are insensitive to antinodal quasiparticles.

A potentially powerful approach to studying the interactions of antinodal quasiparticles at low temperature is to create a nonthermal population by external excitation. By

probing the relaxation of the nonthermal population to the ground state, one may hope to learn about interactions between quasiparticles that would not normally be present at low temperature. Time-resolved optical techniques are ideally suited to creating a nonequilibrium density of quasiparticles and measuring their subsequent relaxation. These techniques are based on mode-locked lasers that produce pulses of 10-100 fs duration with a wide range of energy per pulse, center wavelength, and repetition rate. Such measurements are performed in a 'pump-probe' mode in which a beam of pulses is split in two. The pump pulse creates the nonequilibrium state while the probe pulse senses the change in the optical response of the medium due to the nonequilibrium population. The time delay between the two pulses is controlled continuously and accurately by varying the optical path length difference between the two beams. Measuring the transmission or reflection of the probe as a function of time delay gives information about the return to equilibrium after the pulsed excitation.

There have been several time-resolved optical measurements performed on the $YBa_2Cu_3O_{7-x}$ (YBCO) system of cuprate superconductors. The earliest work [23, 11, 8, 4] reported the change in the reflectivity (ΔR) of a 1.5 eV probe due to photoexcitation at the same energy. The measurements showed that in the normal state ΔR is small and decays very rapidly. Upon cooling below T_c, ΔR increases rapidly, and its decay rate decreases. These results suggested that carrier thermalization and/or recombination proceed rapidly in the normal state, but are strongly impeded by the opening of the superconducting gap.

Subsequent measurements provided a more detailed picture of the magnitude and decay rate of ΔR as a function of carrier concentration [10]. In underdoped samples ΔR

is readily detectable in the normal state. The decay rate slows with cooling, suggesting a correlation between the relaxation rate of the nonequilibrium state and the appearance of the pseudogap. It was reported that the relaxation time is insensitive to T in the superconducting state, with the exception of a peak near T_c. The results were interpreted in terms of an excited state in which quasiparticles and phonons rapidly reach quasiequilibrium. The decay rate was conjectured to reflect the thermalization of nonequilibrium phonons.

Recently, measurements of ΔR at 1.5 eV were reported on an untwinned single crystal of $YBa_2Cu_3O_{6.5}$ Ortho II [45]. (The designation Ortho II refers to the macroscopic ordering of the atomic layer containing the Cu-O chains. In the Ortho II phase the chains alternate between fully occupied, and entirely unoccupied, by O atoms). In these measurements the range of pump intensity was extended to nearly two orders of magnitude smaller than used in earlier measurements. It was shown that while the T dependence of the decay rate is weak when the intensity, I, is large, it becomes extremely strong as I is reduced. In fact, the decay rate appeared to vanish as T and I both tend to zero. It was suggested that the strong I dependence of the decay rate is not consistent with a picture in which the quasiparticles and phonons reach quasiequilibrium and an alternate mechanism involving the pairwise scattering of quasiparticles was suggested.

In this chapter, we present further measurements and analysis of time-resolved photoinduced reflectivity in YBCO Ortho II. The experimental apparatus and sample characterization are described in Section 3.2. In Section 3.3 we introduce the Rothwarf-Taylor (RT) equations, which provide a phenomenological framework for interpreting nonequilibrium dynamics in superconductors. Section 3.4 presents measurements of the decay of the

photoinduced reflectivity as a function of time, temperature, and pump beam intensity. The essential experimental finding, as in Ref. [45], is that the characteristic decay time diverges as both T and I approach zero. However, we present several results beyond those already reported. We present and analyze the time dependence of the transient reflectivity, showing that it is described well by the pairwise scattering of quasiparticles. Second, we report improved measurements of the asymptotic value of the decay rate in the limit that I goes to zero. Through improvements in sensitivity we were able to measure γ_{th} with more than one order of magnitude greater precision than previously. Finally, in Section 3.5 we present analysis and interpretation of the experimental results. We argue that the quasiparticles that give rise to ΔR are antinodal in character and interpret the decay rate as a measure of the strength of antinodal quasiparticle interactions.

3.2 Experimental methods

Pump and probe measurements were performed on a mechanically detwinned single crystal of $YBa_2Cu_3O_{6.5}$ with T_c=45 K. The sample was grown in a $BaZrO_3$ crucible, which yields material with purity at the 0.99995 level. The high purity allows allows the development of very long correlation lengths ($\xi_a = 148\mathring{A}$, $\xi_b = 430\mathring{A}$, $\xi_c = 58\mathring{A}$) of Ortho II order [36], in which the the charge reservoir layer consists of alternating filled and empty copper oxygen chains. Together with $YBa_2Cu_4O_8$, it is one of two underdoped cuprate superconductors in which doping does not introduce disorder. The relative lack of disorder is reflected in the low temperature transport properties, which indicate quasiparticle scattering times in excess of 30 ps [48].

In our experiments, the pump and probe beams were produced by a mode-locked Ti:Sapphire laser. The pulses have duration 100 fs, repetition rate 90 MHz, and center wavelength 800 nm. Both pump and probe beams were focused onto the sample with a 20 cm focal length lens, yielding a spot size of 75 μm diameter. The reflected probe beam was focused onto a Si photodiode detector.

A double modulation scheme was used to optimize sensitivity to small changes in the power of the reflected probe beam. In order to minimize the noise from the Si photodiode detector, a photoelastic modulator was used to modulate the amplitude of the pump beam at 100 KHz. In addition, a galvanometer-mounted mirror varied the path-length difference between pump and probe beams at a frequency of 40 Hz. This yields a rapid scan of the time delay between pump and probe, which helps to suppress noise due to 1/f fluctuations of the probe beam power. In order to demodulate and extract ΔR as a function of time delay, the output of the Si photodiode was sent to a lock-in amplifier for phase-sensitive detection of the 100 KHz component. The output of the lock-in was then sent to a digital oscilloscope whose time base was triggered synchronously to the oscillating mirror. With the oscilloscope in averaging mode, a minimum detectable $\Delta R/R$ of $\approx 10^{-7}$ could be achieved after approximately 10 minutes of accumulation time. More details about our setup can be found in Chapter 2.

In this study, we focused on the decay rate of ΔR immediately following the pulsed excitation, or $\gamma(0)$. For most of the measurements, we determined $\gamma(0)$ by fitting $\Delta R(t)$ at small time delays by a decaying exponential. However, special considerations arose in measurements of $\gamma(0)$ at very low pump power. As described in succeeding sections, $\gamma(0)$

decreases as the pump intensity is lowered. At low temperatures, the decay rate decreases to the extent that the change in ΔR over the 25 ps time delay range produced by the oscillating mirror is extremely small. To measure $\gamma(0)$ in this regime, we switched to a detection scheme that probes directly the derivative of ΔR with respect to time delay. The signal from the first lock-in was sent to a second lock-in, rather than the digital oscilloscope, for phase-sensitive detection at the frequency of the oscillating mirror. When the oscillating time delay is less than the decay time of ΔR, the output of the second lock-in is proportional to the derivative $d\Delta R/dt$. In this mode of data acquisition we vary the pump-probe delay by a conventional system of a retroreflector mounted on a translation stage.

When measured at low pump intensity, $\gamma(0)$ is remarkably sensitive to T, decreasing about an order of magnitude between 15 and 10 K, for example. The extreme sensitivity to temperature suggests that laser heating can introduce significant error in determining the T-dependence of $\gamma(0)$. (By laser heating we refer to the steady-state increase in sample temperature due to the time-averaged laser power). For the experiments described above, the pump intensity was lowered below the intensity of the probe. In this regime, the probe beam is responsible for heating the photoexcited region. At low temperature we can readily observe that $\gamma(0)$ varies as the probe intensity, and consequently the sample temperature, is varied. The obvious remedy of reducing the probe power has the drawback that the ΔR signal soon disappears below the detector noise level.

Empirically, we found that the optimal compromise between signal-to-noise ratio and laser heating is obtained at a probe power of approximately 1.2 mW. At this power level $\gamma(0)$ can be measured, yet the induced temperature change is significantly less than

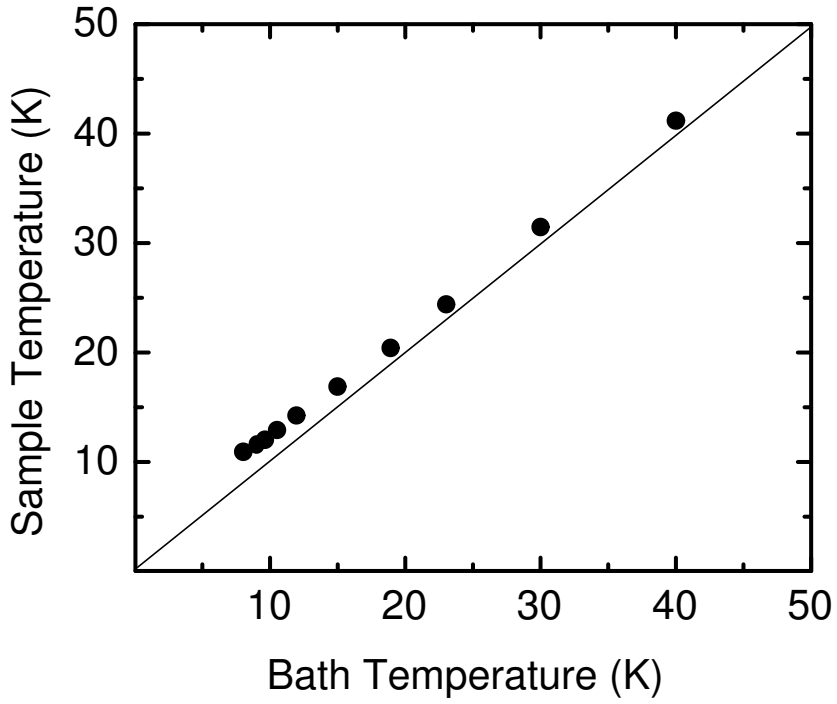

Figure 3.1: Temperature of the photoexcited region of the sample as a function of the bath temperature, as determined by numerical simulation.

the bath temperature. Determining the dependence of $\gamma(0)$ on T at this power level requires that we know the temperature of the photoexcited region of the sample. Unfortunately it is extremely difficult to measure, with the required accuracy, the temperature of the sample directly under the focal spot.

Because of this difficulty, we have performed a numerical simulation of the thermal diffusion equation to estimate the laser-induced temperature change. We input to this simulation a realistic model for the thermal properties of the sample and its coupling to the bath. In the experiment, the sample is attached to a sapphire plate using thermal grease. After mounting, the thickness of the grease layer is determined using an optical

microscope. The input parameters to the numerical simulation are the thicknesses of the sample and grease layer, as well as their temperature dependent thermal conductivities [22, 32, 31]. Figure 3.1 shows the temperature of the photoexcited region as a function of the bath temperature, as determined by finite-element analysis of the diffusion equation. In the simulation, the laser power is 1.2 mW, focused to a spot of diameter 75 μm. The thickness of the sample and thermal grease were 20 μm and 5 μm, respectively. In the subsequent analysis of the low-pump intensity data, we used the calculated temperature, rather than the temperature of the thermal bath.

3.3 Background: Rothwarf-Taylor equations and the phonon-bottleneck

In this section we introduce the Rothwarf-Taylor [44] equations, which provide a successful phenomenological framework for understanding nonequilibrium dynamics in superconductors [21]. The RT equations are a pair of rate equations that describe a system of superconducting quasiparticles coupled to phonons. In the RT phenomenology the excited state is characterized by number densities rather than nonequilibrium energy distribution functions. This drastic simplification is justified in s-wave superconductors because quasiparticles rapidly thermalize to a narrow range of energy just above the gap. In d-wave superconductors the time evolution of the quasiparticle distribution function may be more complicated. In spite of this, we have found that the RT equations provide an excellent description of the dynamics of YBCO Ortho II after pulsed photoexcitation. In the final section we comment on the underlying reasons for the applicability of the RT approach.

In this work we write the RT equations in the following form,

$$\dot{n} = I_{qp} + 2N\gamma_{pc} - \beta n^2 \tag{3.1}$$

$$\dot{N} = I_{ph} + \beta n^2/2 - \gamma_{pc}N - (N - N_{eq})\gamma_{esc} \tag{3.2}$$

where n, and N, are the number densities of gap energy quasiparticles and phonons, respectively. The right hand side of Eq. 3.1 expresses the difference between the rates of quasiparticle creation and annihilation. I_{qp} is the external generation rate and $2N\gamma_{pc}$ is the rate of pair creation *via* annihilation of gap energy phonons. The quasiparticle annihilation rate βn^2 varies quadratically with density because recombination is a two-particle scattering event. In Eq. 3.2 the time rate of change of the phonon density is given by the external phonon creation rate and the same recombination and pair creation terms (with opposite signs) as in Eq. 3.1. The parameter γ_{esc}, which appears in the last term in Eq. 3.2, is the rate at which a gap energy phonons are removed from the interacting system. This can occur either because of decay into below-gap energy phonons that cannot regenerate a quasiparticle pair, or diffusion out of the excited volume. Although for conventional superconductors the escape process is relatively slow, it is essential for the ultimate return of the coupled system to equilibrium.

Here we are concerned with the evolution of the system following pulsed excitation. In general, the time evolution depends on the relative magnitude of the three critical parameters, γ_{esc}, γ_{pc}, and β. Typically, $\gamma_{esc} \ll \gamma_{pc}$, which is the limit where a gap energy phonon is far more likely to regenerate a quasiparticle pair than to decay into the bath. In this case the phonon population will increase following photoexcitation until quasiequi-

librium between phonons and quasiparticles is established. The onset of quasiequilibrium occurs when the pair creation rate $\gamma_{pc}N$ becomes approximately equal to the recombination rate βn^2. For earlier times, where $\gamma_{pc}N \ll \beta n^2$ the quasiparticle population decays at the density dependent rate βn. However, once quasiequilibrium is established the two populations are strongly coupled. In this regime N and n both decay at the much slower rate γ_{esc}. The subsequent decay of the quasiparticle population is slow and independent of density, despite the fact that the rate of quasiparticle scattering may be rapid and density dependent. The limit on the decay of the nonequilibrium quasiparticle density imposed by the quasiequilibrium with the phonons is termed the phonon bottleneck.

3.4 Experimental results

3.4.1 Intensity dependence at low temperature

The decay rate of the photoinduced reflectivity in YBCO Ortho II depends strongly on both the temperature, T, and the pump intensity, I. Fig. 3.2 illustrates the increase of the decay rate with increasing I at a fixed T=9 K. Each curve, measured using a different I in the range from 0.5 to 25 mW, has been normalized to the same value at $t = 0$ to illustrate the variation in decay rate.

Before analyzing the intensity dependence of the decay rate we return briefly to the question of laser-induced heating. As we will discuss in detail in Section 3.4.2, the decay rate measured at fixed pump intensity increases rapidly with temperature. This raises the concern that the intensity dependence of the decay rate shown in Fig. 3.2 is an artifact of pump-induced heating. The decisive test is the behavior of the decay rate as the pump

power is varied from above to below the probe power. In the regime where the pump power is greater than that of the probe, T increases with I. However, in the regime where the pump power is less than the probe power, T becomes independent of I. Therefore an explanation of intensity dependence in terms of heating would predict a crossover to an I-independent decay rate when the pump power becomes less than that of the probe.

The dashed curve in Fig. 3.2 shows the decay of ΔR when both pump and probe powers are equal to 2.5 mW. The slowing of the decay rate continues without any sign of crossover as I is lowered ultimately to 0.5 mW, which is one-fifth of the probe power. Thus the intensity dependence of the decay rate persists into a regime where I cannot influence the sample temperature. These data show that the dependence of decay rate on power is intrinsic and not the result of heating of the sample by the laser. As we have discussed previously, when the pump intensity increases well above that of the probe the sample temperature will increase. Ultimately, at high values of I the effects of temperature and intensity on the decay rate will become mixed. However, all of the quantitative analysis in this chapter is based on the behavior of the decay rate in the low pump-intensity limit.

The variation in decay rate with excitation density observed in YBCO Ortho II is highly unusual. Analogous experiments on s-wave superconductors have consistently found that the decay rate of the nonequilibrium state is independent of the quasiparticle density [21]. The lack of density dependence is understood as a manifestation of the phonon bottleneck effect. As discussed in the previous section, the bottleneck sets in when $\gamma_{pc}N$ reaches approximately βn^2. If there is no significant recombination on this time scale, then only density-independent bottleneck dynamics can be seen.

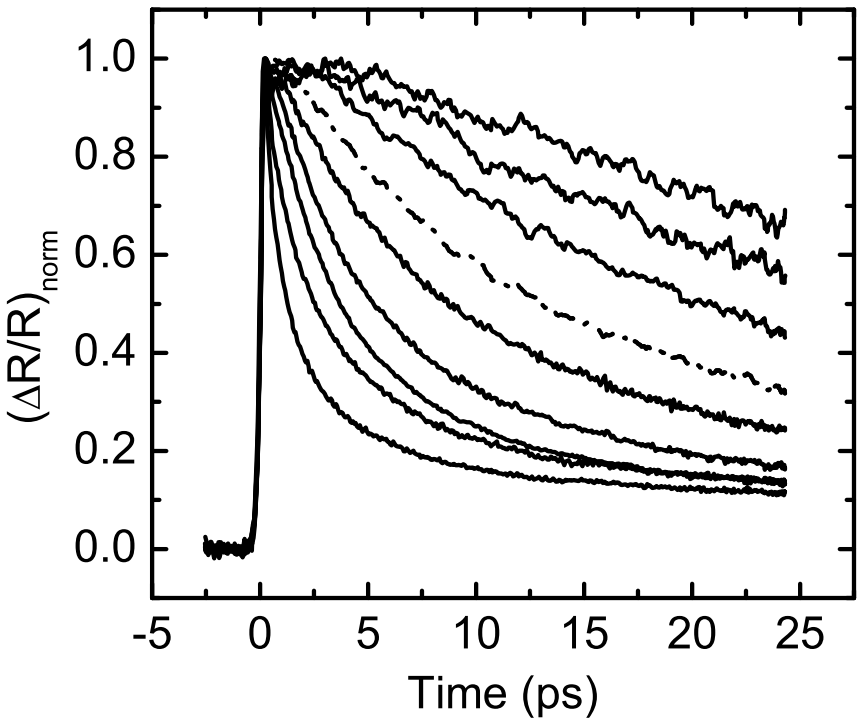

Figure 3.2: $\Delta R/R$ at T=9 K as a function of time following pulse excitation, for several pump intensities. All curves were normalized to the same value at delay time zero to illustrate the variation in initial decay rate. The most rapid decay is seen at the highest pump intensity, corresponding to 25 mW of laser power focused to spot of diameter $75\mu m$. The decay becomes systematically slower as the pump intensity is reduced by factors 0.69, 0.44, 0.24, 0.15, 0.10, 0.06, 0.04 and 0.02. The dashed curve (attenuation factor 0.10) corresponds to a pump intensity equal to that of the probe.

The observation that the decay rate depends on density suggests the absence of a phonon bottleneck on the time scale of our measurements. In Section 3.5.4 we discuss in detail under what circumstances this can occur. Briefly, what is required is that the rate $\gamma_{pc}N$ remains smaller than βn^2. This can happen in either one of two regimes. In the first regime, γ_{pc} is very small on the scale of maximum quasiparticle recombination rate $\beta N(0)\Delta$. In this case, the quasiparticle density will decay to a small fraction of its initial

value before steady-state equilibrium is reached. In the second regime, the hierarchy of pair creation and escape rates is reversed, such that $\gamma_{pc} \ll \gamma_{esc}$. In this case the phonon population is drained off before a quasi-steady state with the electronic excitations can be achieved.

If, in fact, the decays that we observe are free of phonon bottleneck effects, the measured rates provide direct information about the size of the coefficient β. This in turn offers a window into the nature of quasiparticle-quasiparticle scattering. To test whether our measurements of YBCO Ortho II are in a non-bottleneck regime, we have analyzed the time-dependence of the decay of ΔR. Fig. 3.3 is a double log plot of ΔR as a function of time delay, for several pump intensities. At the highest excitation density ΔR decays as a power law for $t > 3$ ps. With decreasing excitation density the onset of power law decay shifts to longer times. At the lowest intensity the crossover time is greater than the maximum time delay in this set of measurements, which is $\sim$25 ps. We compare these curves with the predictions of the RT equations in the parameter regime in which the quasiparticles and phonons remain out of equilibrium. The RT equations are clarified if the total quasiparticle population is written as $n_{ph} + n_{th}$, where n_{ph} and n_{th} are the photoinduced and thermal equilibrium quasiparticle density, respectively. Similarly, we define N_{ph} and N_{th} as the photoinduced and thermal equilibrium phonon populations. Detailed balance relates the thermal densities of phonons and quasiparticles such that $2N_{th}\gamma_{pc} = \beta n_{th}^2$. Substituting the above relation into Eq. 3.1 yields a rate equation for n_{ph},

$$\dot{n}_{ph} = I_{qp} - \beta n_{ph}^2 - 2\beta n_{th} n_{ph} + 2\gamma_{pc} N_{ph}. \tag{3.3}$$

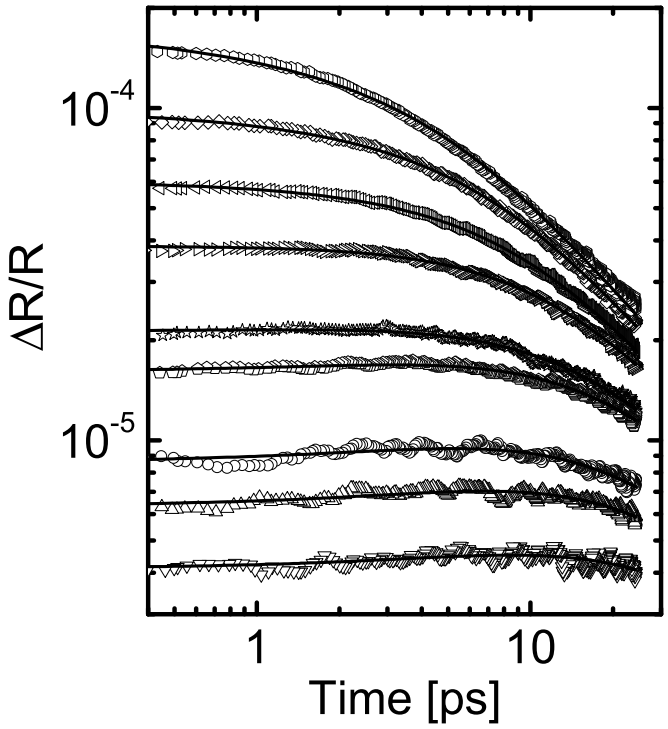

Figure 3.3: $\Delta R/R$ *vs.* time delay at T=9K plotted on a double logarithmic scale, for pump laser powers (in mW) 0.1, 0.2, 0.4, 0.6, 1.0, 1.5, 2.4, 3.8, 6.0.

If either condition $\gamma_{pc} \ll \beta N(0)\Delta$ or $\gamma_{pc} \ll \gamma_{esc}$ is satisfied, the last term in Eq. 3.3 may be ignored, which leads to decoupling of the two RT equations. The resulting rate equation for the quasiparticles,

$$\dot{n}_{ph} = I_{qp} - \beta n_{ph}^2 - 2\beta n_{th} n_{ph}, \tag{3.4}$$

becomes equivalent to the rate equation applicable to nonequilibrium electrons and holes in semiconductors, and has been studied extensively in connection with photoconductivity [5]. If n_{th} vanishes as T approaches zero, then the rate equation approaches $\dot{n}_{ph} = I_{ph} - \beta n_{ph}^2$.

At low T the quasiparticles obey simple second order, or bimolecular, reaction kinetics. Integration yields the decay after pulsed excitation,

$$n_{ph}(t) = \frac{n_{ph}(0)}{[1 + \beta n_{ph}(0)t]}. \tag{3.5}$$

Eq. 3.5 predicts that the excited population approaches $1/\beta t$ for $t \gg 1/\beta n_{ph}(0)$, regardless of the initial quasiparticle density. However, as is clear from Fig. 3.3, the measured decay curves do not obey this prediction. At long times the decay is closer to $t^{-0.8}$ than t^{-1}, and curves for different intensities do not merge to a single curve at long times.

The discrepancies described above can be traced to a complication omitted from the preceding analysis. Because the intensity of the pump beam decreases exponentially with increasing depth below the sample surface, z, the local quasiparticle density, $n_{ph}(z,t)$, is spatially nonuniform. The initial local density $n_{ph}(z,0)$, equals $n_{ph}(0,0)e^{-\alpha z}$, where α is the absorption coefficient at the pump wavelength. Assuming negligible diffusion of excitations in the z direction, the local excitation density decays as,

$$n_{ph}(z,t) = \frac{n_{ph}(z,0)}{[1 + \beta n_{ph}(z,0)t]}. \tag{3.6}$$

The probe beam, whose change in reflectivity measures the excited quasiparticle density, also decays exponentially in the sample. Therefore the measured reflectivity change is related to an exponentially weighted average of the nonequilibrium quasiparticle density,

$$\mathcal{N}(t) \equiv \alpha^{-1} \int_0^\infty dz e^{-\alpha z} n_{ph}(z,0)/[1 + \beta n_{ph}(z,0)t]. \tag{3.7}$$

Assuming that the change in reflectivity is proportional to $\mathcal{N}$ finally yields,

$$\Delta R(t) = \frac{2\Delta R(0)}{\gamma_0 t}[1 - \frac{ln(1+\gamma_0 t)}{\gamma_0 t}], \tag{3.8}$$

where $\gamma_0 \equiv \beta n_{ph}(0,0)$.

The solid lines in Fig. 3.3 indicate the best fit of Eq. 3.8 to the experimental data. The fit is obtained by varying $\Delta R(0)$ and γ_0 for each curve. There is excellent agreement between the data and the prediction of the bimolecular rate equation when the exponential variation of the pump and probe intensities is taken into account. The agreement suggests that for $t < 25$ ps, the phonon bottleneck is not established and the decay rate of ΔR is a direct measure of the quasiparticle-quasiparticle scattering rate.

From the fitting procedure we determine $\Delta R(0)$ and γ_0 for each curve. In Fig. 3.4 we plot γ_0 as a function of $\Delta R(0)/R$. It is evident that the characteristic decay rate increases *linearly* with the magnitude of the initial reflectivity change. The linear relationship indicates that the entire family of decay curves can be described by a single bimolecular coefficient β.

3.4.2 Temperature dependence

In the previous section we showed that the decay of ΔR at low temperature can be described by the bimolecular rate equation with a single value of the scattering coefficient β. In this section we analyze the effect of raising the temperature on the rate of decay of ΔR. Fig. 3.5 shows a set of normalized decay curves of ΔR, measured in the temperature range from 5-70 K, induced by a pump power of 2.5 mW. The set of curves illustrates clearly that the decay rate at fixed I increases rapidly with increasing T.

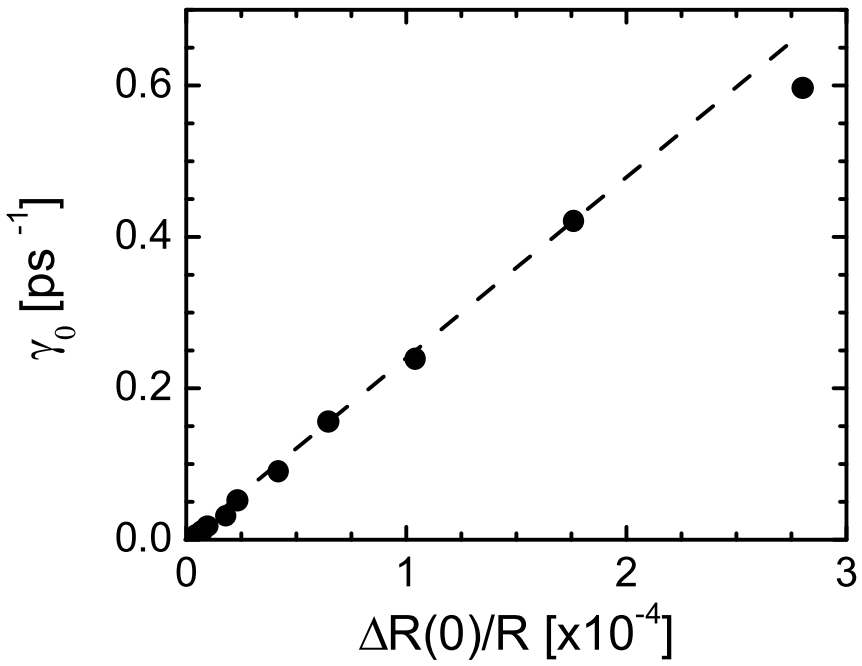

Figure 3.4: The initial decay rate at the sample surface, γ_0, as a function of the initial reflectivity change, $\Delta R(0)/R$. The dashed line emphasizes the linear dependence of initial decay rate on initial density.

To analyze the T dependence, we again consider the RT equation in the decoupled regime (Eq. 3.4). At nonzero T we must include the last term on the right-hand side, which was neglected previously. Physically, this term describes the rate of scattering of a photoinjected quasiparticle by a thermal equilibrium one.

We have found that the most direct way to compare the data with Eq. 3.4 is to focus on the initial decay rate, $\gamma(0)$, of the experimentally measured transients. Here $\gamma(0)$ is defined as the limit of the instantaneous decay rate $\gamma(t) \equiv -\dot{n}_{ph}/n_{ph}$ as t approaches zero. According to Eq. 3.4, $\gamma(0) = \beta\,[n_{ph}(0) + 2n_{th}]$. Assuming that the initial reflectivity change is proportional to $n_{ph}(0)$, a plot of $\gamma(0)$ vs. $\Delta R(0)$ should yield a straight line with

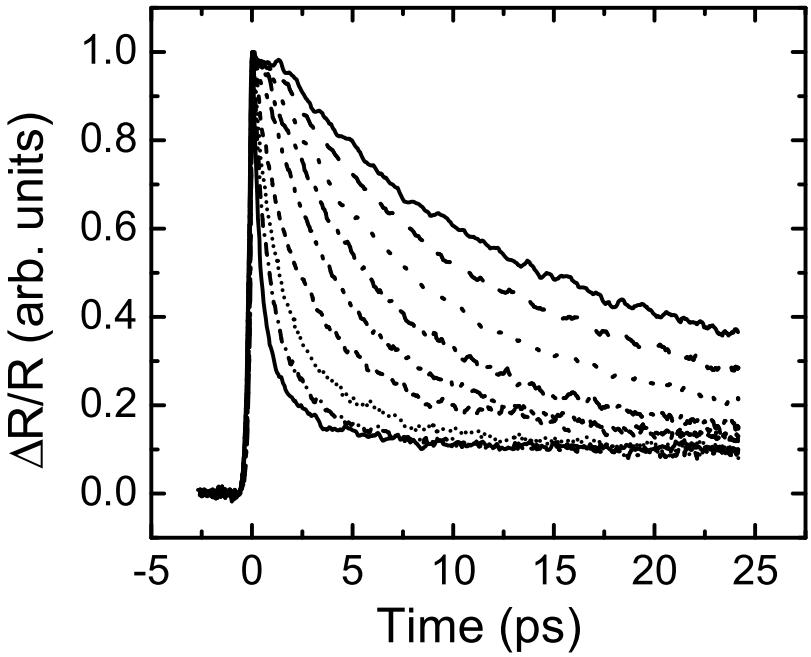

Figure 3.5: $\Delta R/R$ induced by 2.5 mW of laser power, as a function of time following pulse excitation, for several temperatures in the range from 5-70 K. All curves were normalized to the same value at delay time zero to illustrate the variation in initial decay rate. The decay is most rapid at the highest temperature, and becomes systematically slower as T is reduced from 70 K to 50 K, 44 K, 28 K, 22 K, 17 K, 12 K, and 5 K.

slope proportional to β and intercept $2\beta n_{th}$.

Fig. 3.6 shows $\gamma(0)$ plotted as a function of $\Delta R(0)/R$ for several temperatures in the superconducting state. The data at the lowest temperature are essentially equivalent to the results presented earlier. In Fig. 3.4 the decay rate was determined by fitting the entire time dependence, while in Fig. 3.6 the decay rate is determined from the initial slope. The reason the decay rates in the two figures differ by a factor of two can be understood from Eq. 3.8. Taking the derivative of this formula with respect to time shows that $\gamma(0) = \gamma_0/2$.

With increasing T the $\gamma(0)$ vs. $\Delta R(0)$ plots shift vertically, with little change

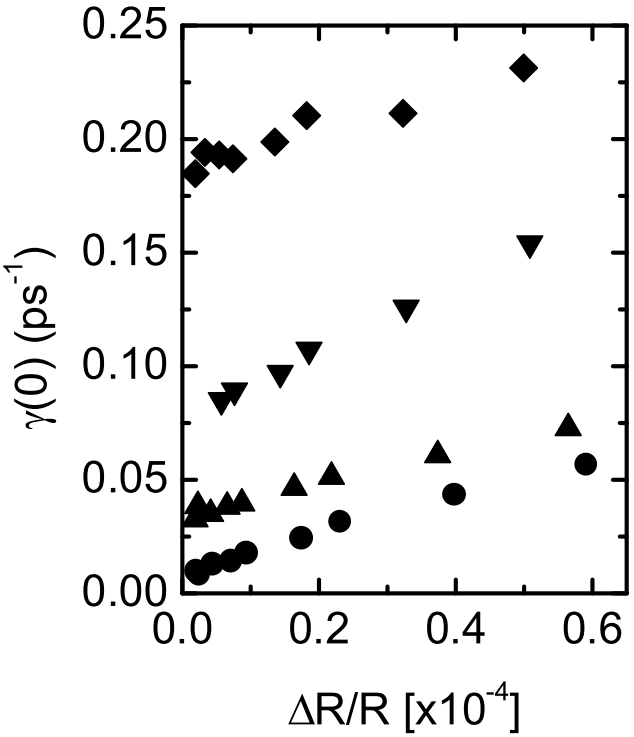

Figure 3.6: Initial decay rate, $\gamma(0)$, as a function of initial reflectivity change, $\Delta R(0)/R$, for T=12 K, 17 K, 22 K, and 30 K. The thermal equilibrium decay rate, obtained from extrapolation of the data to zero $\Delta R(0)/R$ increases rapidly with temperature.

in slope. The fact that the slope is nearly constant implies that β depends weakly, if at all, on the temperature. The increase of the intercept with T implies a rapidly increasing density of thermal equilibrium excitations. In the next section we examine the temperature dependence of the intercepts, as determined from measurements performed at very low pump and probe intensities.

Fig. 3.7 presents a different perspective of the decay rate as a function of temperature and intensity: $\gamma(0)$ as a function of T for three values of I. In the normal state and just below T_c the different data sets lie on the same curve, indicating that $\gamma(0)$ is independent of I. As the temperature is lowered below T_c the decay rates measured with

different pump intensities begin to diverge. As the temperature tends to zero, the decay rate crosses over to a temperature independent regime, with the crossover temperature higher when the rates are measured at greater pump intensity. A consistent explanation for the T and I dependence of $\gamma(0)$ can be found in the picture of pairwise scattering involving both thermal equilibrium and photoinduced quasiparticles. The lack of intensity dependence above T_c suggests that in this regime the thermal density of quasiparticles is far larger than the photoinduced density. The strong temperature dependence above T_c suggests that n_{th} decreases with decreasing temperature in the normal state, possibly due to the opening of the pseudogap. The onset of intensity dependence at T_c may indicate that n_{th} has become comparable to n_{ph}. Alternatively, the sudden change in decay kinetics may be related to the onset of the coherence in the antinodal quasiparticle self-energy. Finally, the decay rate measured at fixed pump intensity crosses over to T-independence when n_{th} becomes much smaller than $n_{ph}(T)$. The overall behavior of $\gamma(0)$ suggests that the decay rate vanishes in the limit that both I and T go to zero.

3.4.3 Low intensity regime

In this section we focus on measurements of $\gamma(0)$ performed at the lowest laser intensities that are accessible experimentally. The motivation for studying the low-intensity regime is to measure, *via* a nonequilibrium experiment, the recombination lifetime of quasiparticles in equilibrium. In order to probe equilibrium properties, the density perturbation introduced by the laser must be small, such that $n_{ph} \ll n_{th}$. According to Eq. 3.4, $\gamma(0)$ approaches $2\beta n_{th}$ in this limit, which is exactly twice the thermal equilibrium recombination rate, γ_{th}.

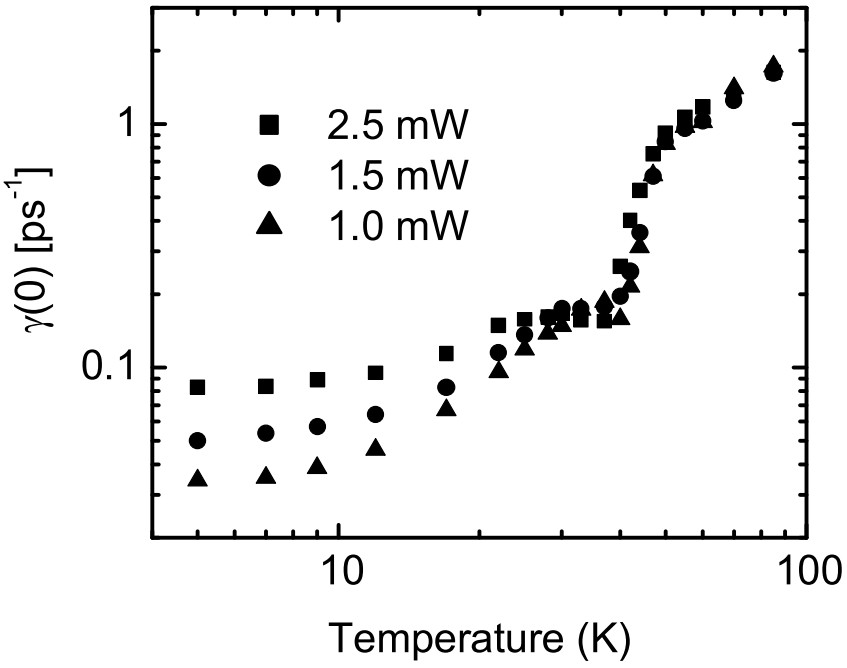

Figure 3.7: Initial decay rate, $\gamma(0)$, as a function of T for three values of pump power.

Measuring γ_{th} accurately becomes increasingly difficult at low temperature because of the requirement that $n_{ph} \ll n_{th}$. As n_{th} decreases rapidly with decreasing T, the pump intensity must be lowered accordingly. Eventually ΔR reaches the noise floor of the experiment, which sets a limit on the smallest γ_{th} that can be measured. In principle, the signal size could be increased by raising the intensity of the probe beam. However, this inevitably leads to an increase in the average temperature of the photoexcited region compared with the bath temperature. This problem becomes increasingly severe at low temperature, where the thermal conductivity of the sample is small. For the data to be presented, the probe intensity was maintained at 1.2 mW, a value which provides the best compromise between sensitivity and heating.

At each T, we obtain $2\gamma_{th}$ from the extrapolation to zero of a linear fit to $\gamma(0)$ vs. ΔR. The temperature of the photoexcited region is determined through the numerical analysis described in Section 3.2. Fig. 3.8 is a double logarithmic plot of $2\gamma_{th}$ as a function of T, showing results for both YBCO Ortho II and a thin film sample of $Bi_2Sr_2CaCu_2O_8$ (BSCCO) [46]. At the upper limit of the T range, γ_{th} is nearly identical in the two materials. However, as mentioned previously, the dependence of γ_{th} on T becomes very strong in YBCO Ortho II at low temperature. If the functional form was assumed to be a power law, then γ_{th} would approach a T^8 dependence.

We believe it to be more reasonable to assume that γ_{th} in YBCO Ortho II decreases exponentially at low temperature. To analyze this exponential dependence, we compare the data with the formula,

$$2\gamma_{th}(T) = \frac{k_B T}{\hbar}\frac{T}{T_0} exp\left[-\Delta_{th}(T)/k_B T\right]. \tag{3.9}$$

We introduce a prefactor proportional to T^2 for two reasons, one theoretical and the other experimental. The theoretical reason is that $n_{th}(T)$ is predicted to vary as T^2 for a d-wave superconductor. The experimental reason is that in some samples of BSCCO γ_{th} is proportional to T^2 over the temperature range from 10 K to 40 K [46]. (The dashed line in Fig. 3.8 indicates a T^2 dependence). Fitting Eq. 3.9 to the YBCO Ortho II data yields $T_0 = 1100$ K and a temperature dependent activation energy Δ_{th} that is plotted in the inset. The origin of the exponential cutoff in γ_{th} that appears in YBCO Ortho II and not in BSCCO is not understood at present. However, we note that analogous behavior is observed in the scattering rates observed by ac conductivity experiments. In the YBCO system, the mean

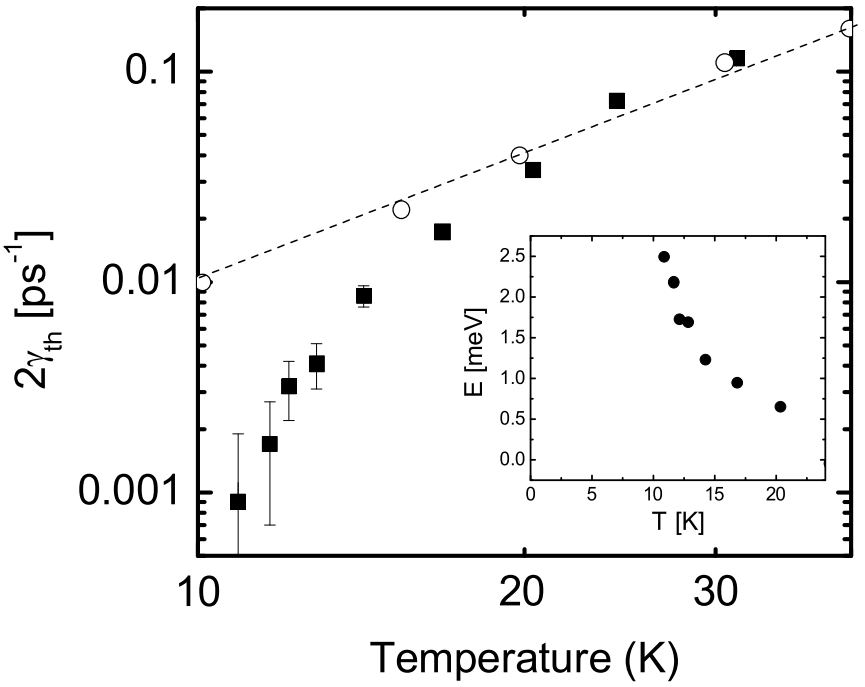

Figure 3.8: Twice the thermal equilibrium recombination rate, as determined by the extrapolation of $\gamma(0)$ to zero laser power, as a function of temperature. Solid squares are results for the YBCO Ortho II sample, open circles show results obtained on a thin film sample of BSCCO with T_c= 85 K. The dashed line indicates a temperature dependence proportional to T^2. The inset shows the activation energy of the recombination rate in YBCO Ortho II as determined from a fit to Eq. 3.9.

free path increases exponentially with temperature towards a limit of several microns set by elastic processes [48]. In BSCCO the T dependence is much weaker and the limiting value is only a few hundred $\AA$ [9]. It is possible that momentum conservation imposes constraints on the rate of quasiparticle-quasiparticle scattering in the cleaner YBCO system. These constraints may dictate that only Umklapp processes are allowed at low T, leading to an exponential T dependence [52, 27].

3.5 Discussion

In analyzing the experimental data presented above, we begin (in Section 3.5.1) with the most basic question: what type of excitation is probed by transient reflectivity experiments performed on the cuprate superconductors? We argue that these excitations are quasiparticles that occupy states close to the antinodal regions of the Brillouin zone. In Sections 3.5.2 and 3.5.3 we turn to a quantitative analysis of the decay rate of the photoexcited state. Section 3.5.2 focuses on our observation that the lifetime of a photoinjected quasiparticle diverges in the limit that T and I both tend to zero. We show theoretically that the constraints of momentum and energy conservation prevent thermalization of antinodal quasiparticles toward the nodes. In Section 3.5.3 we estimate the magnitude of the recombination coefficient β from the experimental data, and discuss its theoretical interpretation. Finally, in Section 3.5.4, we comment on possible reasons for the absence of a phonon bottleneck in the decay of the photoexcited state.

3.5.1 What types of excitations are probed?

As a first guess, one might imagine that the photoinduced quasiparticles occupy states near the nodes, as these are the lowest energy excitations. This intuition is consistent with the generally accepted picture of the quasiparticle distribution function in the nonequilibrium state. In this picture the nonequilibrium quasiparticles rapidly adopt a Fermi-Dirac distribution, but with a chemical potential, and temperature, μ^*, and T^*, respectively, that are larger than their values in thermal equilibrium [42, 41]. In a d-wave superconductor this distribution describes a population of quasiparticles that is dominated

by states near the nodes ('nodal' quasiparticles). The occupation of states with energy greater than $\max(\mu^*, T^*)$ is exponentially small.

On the other hand, the experimental evidence suggests that the photoexcited state is not a degenerate gas of nodal quasiparticles. Three observations, in particular, lead us to this conclusion:

(1) *The diffusion coefficient of photoinjected quasiparticles is at least two orders of magnitude smaller than the diffusion coefficient of nodal quasiparticles* [16]. The diffusive propagation of nonequilibrium quasiparticles in YBCO Ortho II was recently measured by the transient grating technique. Values for the diffusion coefficient of 20 cm^2/s and 24 cm^2/s were determined for motion along the **a** and **b** crystalline axes, respectively. This may be compared with a nodal quasiparticle diffusion coefficient of $\approx$ 6000 cm^2/s as determined from microwave spectroscopy on the same sample [48].

(2) *The reduction in the condensate spectral weight depends linearly on the pump intensity.* Information about the photoinduced reduction of condensate spectral weight comes from visible pump-terahertz probe experiments [2]. At frequencies $\sim$1 THz, the optical conductivity $\sigma(\omega)$ is dominated by its imaginary part, σ_2, which is proportional to the condensate density. Following photoexcitation at 1.5 eV, σ_2 drops rapidly as the condensate density is diminished. At intensities below the saturation level, the loss of condensate density is a linear function of the energy deposited in the photoexcited volume.

The linear reduction of condensate density with pump energy is inconsistent with the physics of nodal quasiparticles. This point can be illustrated by considering the temperature dependence of the superfluid density, ρ_s. Nodal quasiparticles are responsible for

the linear in T decrease of ρ_s observed in clean cuprate superconductors [24]. However, the energy stored in the nodal quasiparticle gas increases not as T, but as T^3. Therefore the reduction in ρ_s due to nodal quasiparticles varies as the one-third power of the total energy in the quasiparticle gas. We would expect such a strongly sublinear relationship for a degenerate gas of nonequilibrium nodal quasiparticles as well.

(3) *Far-IR measurements of the photoexcited state show that the optical spectral weight that is removed from the condensate by photoexcitation shifts to energies on the order of 50-100 meV, or several times the value of the maximum gap* [29]. As discussed above, thermal excitation of nodal quasiparticles does indeed remove spectral weight from the condensate. However, the spectral weight shifts to a very narrow ($<30\mu$eV) Drude peak centered on $\omega = 0$. In contrast, the spectral weight removed from the condensate by photoexcitation shifts to frequencies that are $\approx$1000 times higher than the width of the nodal quasiparticle Drude peak. This is further evidence against a degenerate gas of nodal quasiparticles.

On the basis of the preceding arguments, we conclude that nodal quasiparticles do not dominate the population of quasiparticles created by photoexcitation. In other words, the quasiparticle distribution in the photoexcited state cannot be described as a Fermi-Dirac function with effective parameters μ^* and T^*. The experiments are more consistent with a distribution function that is peaked at an energy above the chemical potential. Such a distribution can arise if it is not possible to scatter into the the nodal states during the lifetime of the photoexcited state. In Section 3.5.2 we show that the constraints of energy and momentum conservation severely restrict the rate at which hot quasiparticles scatter

into states near the nodes.

3.5.2 Stability of an isolated photoexcited particle

In section 3.5.1, we argued that the quasiparticle distribution function in the photoexcited state peaks at an energy above the chemical potential and therefore is not of the Fermi-Dirac form. Such a nonequilibrium distribution can arise if quasiparticles cannot scatter into nodal states during the lifetime of the photoexcited state. However, we have also shown that this lifetime can be very long, reaching ~ 0.6 ns at the lowest temperature and intensity accessible experimentally. By comparison a 30 meV excitation in a Fermi liquid (with Fermi energy ~ 1 eV) would decay into electron-hole pairs in $\sim$3 ps. In the following we describe how the relative stability of a quasiparticle in a d-wave superconductor can arise from the severely restricted phase space for decay.

In a Fermi liquid, quasiparticles readily decay into particle-hole pairs because energy and momentum can be conserved in the process. However, the kinematic constraints are much more severe in the case of a d-wave superconductor. Consider the momentum-resolved particle-hole excitation spectrum in the two cases. In the Fermi liquid the particle-hole spectrum forms a broad continuum that extends from zero wavevector to twice k_F, even as the pair energy tends to zero.

The d-wave superconductor differs from the Fermi liquid in that the Fermi contour shrinks to four nodal points. As a consequence, the two-particle excitation spectrum is much more localized in momentum space. Fig. 3.9 illustrates the momentum-resolved two-particle excitation spectrum of a d-wave superconductor. Each plot is a color-scale depiction of the density of two-particle excitations of a given energy in the first Brillouin zone. The spectra

were calculated using a parameterization of the quasiparticle dispersion obtained by Norman [40] from a fit to ARPES data. The value of the maximum gap Δ_0 was arbitrarily set to 50 meV. The conclusions we reach based on the simulation do not depend on the chosen value for Δ_0. At very low energies, the two-particle spectrum is localized near nine discrete wavevectors that represent the creation of particles at the nodes. As the energy of the pair increases, the locus of possible wavevectors spreads out. However, for energies that are less than Δ_0, the allowed momenta remain clustered near the nine zero-energy wavevectors.

In order for a single quasiparticle to scatter and emit a pair of additional quasiparticles, its change in energy and momentum, $\Delta\epsilon$ and Δk, must match that of the pair, ϵ_{pair} and k_{pair}. The constraints imposed by this condition are illustrated in the diagrams shown in Fig. 3.10, which describe the possible decay events of a hot quasiparticle. For this example we have chosen a quasiparticle with energy 40 meV and momentum on the Fermi contour of the normal state. Each diagram corresponds to a fixed energy transfer in the scattering event. The color scale indicates the location of allowed values of Δk and k_{pair} at the transfer energy. A scattering event is kinematically allowed only at momentum transfers where the two sets of wavevectors overlap.

Fig. 3.10 illustrates how kinematics prevent the inelastic scattering of the hot quasiparticle. For example, consider the scattering events with the largest possible energy change, 40 meV. To give up all its energy the hot quasiparticle must scatter to one of the nodes, thus there are only four allowed values of Δk. (The four points are not visible in Fig. 3.10(a)). One of these four wavevectors just touches the perimeter of the elliptical region of pair wavevectors, which indicates an allowed scattering event. In this scattering event

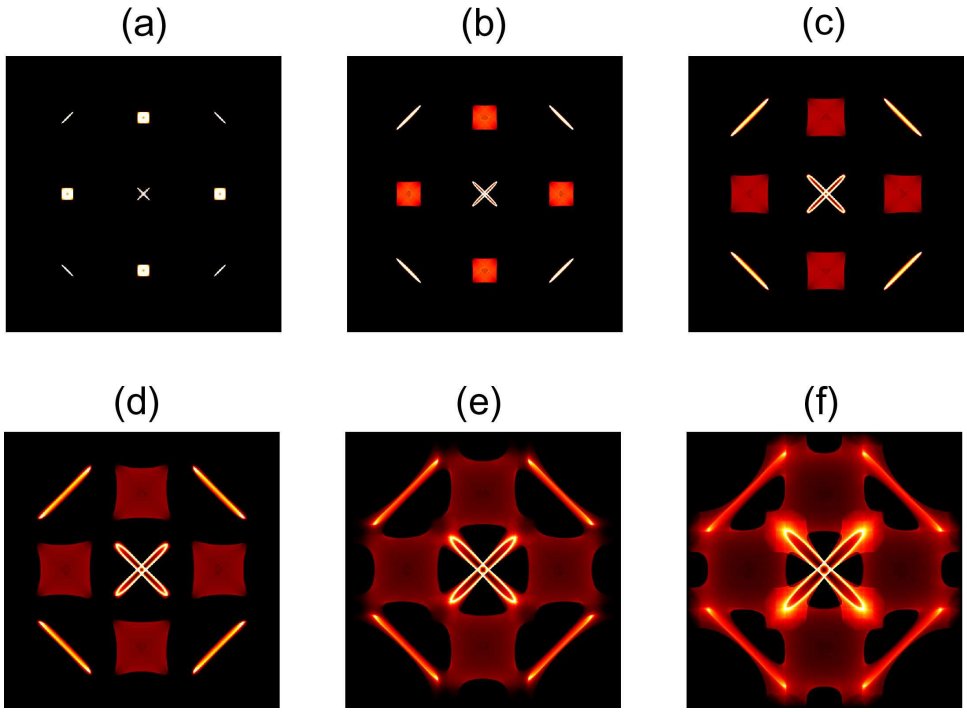

Figure 3.9: Color scale depiction of quasiparticle pair momenta in the first Brillouin zone for different values of the two-particle energy; (a) 10 meV, (b) 20 meV, (c) 30 meV, (d) 40 meV, (e) 50 meV, and (f) 60 meV. The value of the gap parameter Δ_0 is 50 meV.

the hot quasiparticle scatters to the node, with the simultaneous creation of a quasihole at the node and a quasiparticle at the energy and momentum of the hot quasiparticle. This exchange process, although kinematically allowed, does not lead to a change in the particle distribution function.

If the hot quasiparticle does not lose all of its energy, there are more choices for the final momentum. The locus of allowed Δk expands, becoming visible as arcs in panels (b) through (e) of Fig. 3.10. However, as the arcs expand the locus of pair creation wavevectors shrinks. Fig. 3.10 shows that the region of allowed k_{pair} shrinks faster than the expansion of allowed Δk, so that the two regions fail to overlap at any energy transfer less than the energy of the hot quasiparticle. The absence of overlap demonstrates that the thermalization of

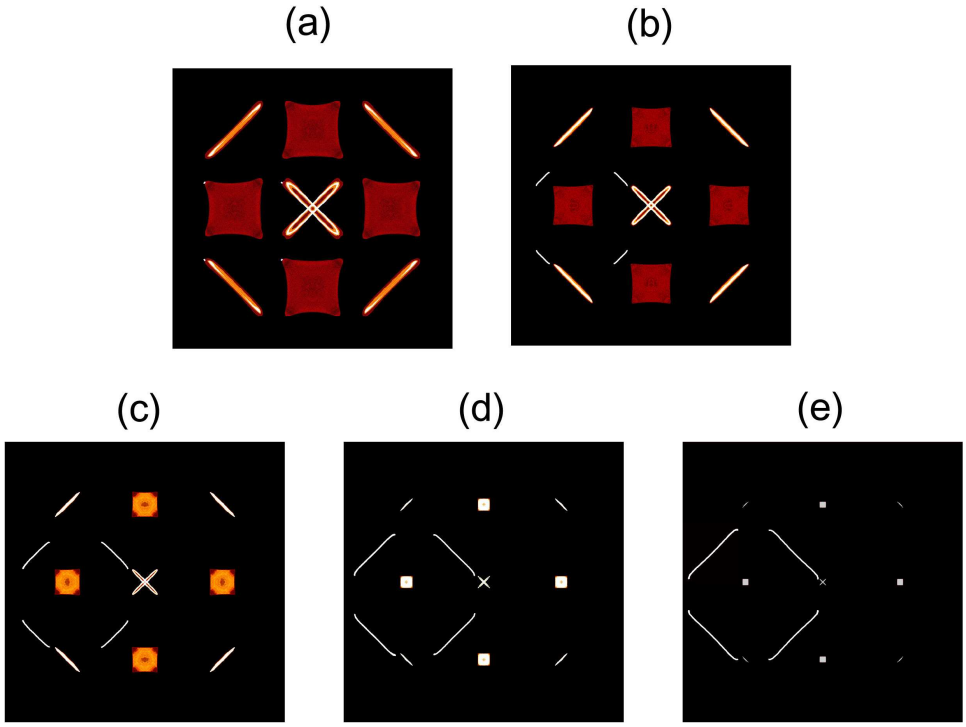

Figure 3.10: Depiction of the lack of overlap between the scattering momentum Δk and the pair momentum k_{pair}. For this illustration the hot quasiparticle starts with energy 40 meV and momentum on the Fermi contour of the normal state. The arc segments in each square show the possible values of Δk for several values of the scattering energy $\Delta\epsilon$: (a) 40 meV; (b) 30 meV; (c) 20 meV; (d) 10 meV; (e) 5 meV. The color scale plot in each of the squares shows the allowed values of k_{pair} at the same energy. As the energy transfer decreases and the arc segments expand, the regions of k_{pair} shrink faster. The lack of overlap is a graphical demonstration of how momentum and energy conservation prevent thermalization of a quasiparticle near the antinodal region of the Brillouin zone.

the hot quasiparticle is forbidden because of kinematic constraints. Recently, Howell et al. [27] reached a similar conclusion based on an analytical, rather than numerical, approach.

The kinematic constraints in this example are specific to quasiparticles near the normal state Fermi contour. They are a consequence of the rapid decrease of quasiparticle velocity with increasing distance from the node. For this reason, we anticipate that not all quasiparticles of a given energy will be stable. The contours of constant quasiparticle energy are distorted ellipses centered on each of the nodes. Quasiparticles near the major axis

vertex of the ellipse will be stable, as we have seen. However, the velocity for particles near the minor axis vertex is comparable the nodal quasiparticle velocity. For these quasiparticles there are no kinematic constraints to prevent rapid thermalization. Thus, we anticipate that after a short time following pulsed injection only nonequilibrium particles near the major axis vertex will survive.

3.5.3 Bimolecular recombination

Estimating β

In the previous section we have seen that kinematic constraints can stabilize an isolated antinodal quasiparticle. However, our experiments show that a *pair* of quasiparticles can convert to a state which no longer contributes to ΔR. We can be confident that this conversion requires two particles, and not more, because the decay rate increases linearly with density. The coefficient that relates the decay rate to the density, β, is directly related to the cross-section for inelastic scattering of two quasiparticles. Thus the magnitude of β is of fundamental importance as a measure of the coupling of quasiparticles to some other excitation of the interacting electronic system.

We turn next to estimating β from the measured dependence of the decay rate on density. Experimentally, we measure both the nonequilibrium decay rate βn_{ph} and the thermal equilibrium rate βn_{th}. To extract β from these measurements, we need to know either n_{ph} or n_{th}. Unfortunately, neither quantity is directly determined from the data, and we need additional assumptions to estimate these quantities. To estimate n_{ph} we use energy conservation to convert from laser energy density to quasiparticle density. In the

linear regime of γ vs. I a recombination rate of 10^{11} s^{-1} results from a laser energy density of 0.1 J-cm^{-3}. If photon energy is converted entirely to 40 meV quasiparticles, then their initial density is $\approx 10^{12}$ cm^{-2}, and therefore $\beta \approx 0.1$ cm^2/s.

We can also determine β from the thermal equilibrium recombination rate as well, if we know $n_{th}(T)$. For a d-wave superconductor,

$$n_{th}(T) = \frac{\pi v_F}{6 v_2} \left(\frac{k_B T}{\hbar v_F} \right)^2, \tag{3.10}$$

where v_F and v_2 are the nodal quasiparticle velocities perpendicular and parallel to the Fermi contour, respectively [7]. Based on the RT equations, we would expect the thermal equilibrium decay rate to be proportional to n_{th} and thus vary with temperature as T^2. Instead, we find experimentally that in YBCO Ortho II the limiting behavior of γ_{th} is exponential rather than power law. The exponential term in the recombination rate suggests that the near-zero energy quasiparticles are not recombining effectively with photoinduced quasiparticles. On the other hand, it is clear that the thermal quasiparticles that do participate need not be antinodal in character because the activation energy of $n_{th}(T)$ is less that one-tenth of the maximum gap value of about 40 meV. The unexpected exponential cutoff of the recombination rate may indicate that only nodal quasiparticles that exceed a small energy, of order a few meV, can participate in recombination. The physics may be related to the small Umklapp scattering gap seen in the momentum scattering rate of nodal quasiparticles [26].

Despite the exponential cut-off of the recombination rate at low T, we can attempt to estimate β from the thermal recombination rate at higher T. Above ≈ 20 K, $\gamma_{th}(T)$ is

not inconsistent with a quadratic dependence on temperature. In that range we found that $2\gamma_{th}(T) \approx (k_B T/\hbar)T/T_0$, with T_0 =1100 K. Assuming that $\gamma_{th} = \beta n_{th}$, and using Eq. 3.10 to estimate $n_{th}(T)$ (with $v_F/v_2 = 10$) we find $\beta = 0.26$ cm^2/s. Considering the approximations and assumptions involved, this value is quite close to the one determined from the nonequilibrium recombination rate.

Theoretical approaches for β

Within the context of BCS theory, the process of recombination is the annihilation of a quasiparticle pair with the simultaneous emission of a gap energy phonon. The theory of the recombination rate of BCS quasiparticles was developed by Kaplan et al. [30], whose calculations assumed an isotropic s-wave gap and the breaking of momentum conservation through strong elastic scattering ('dirty limit'). Their result for the recombination rate, expressed through our definition of recombination coefficient, is $\beta = 4\pi\alpha^2(2\Delta)F(2\Delta)/\hbar N(0)$, where α, F, and N, are the electron-phonon coupling strength, density of phonon states, and density of electron states, respectively. While it is very useful to have this explicit result to compare with, we must bear in mind that the cuprate superconductors do not satisfy the assumptions upon which this calculation is based. The cuprates are 2D rather than 3D, d-wave rather than s-wave, and are in the clean, rather than the dirty, limit of elastic scattering.

We are not aware of a calculation of the phonon-mediated recombination rate applicable to the cuprate superconductors. However, in anticipation of such a calculation, we define a dimensionless constant $C \equiv \hbar\beta N(0)$, that parametrizes the electron-phonon coupling strength in the clean limit. If in addition we express the 2D electronic density

of states through an effective mass m^*, then we obtain the simple formula $\beta = C\hbar/m^*$. Assuming an effective mass that is three times the free electron mass, $\hbar/m^* = 0.3$ cm^2/s, so that $\beta = 0.1$ cm^2/s corresponds to $C \approx 1/3$. It is striking that C is of order unity. This suggests that, while we do not know if phonon emission is indeed the mechanism for quasiparticle recombination, we have identified $\hbar/m^*$ as the 'natural unit' for β.

The body of experimental results on the cuprate superconductors have led many researchers to conclude that quasiparticle scattering is determined by electron-electron, rather than electron-phonon interactions. The BCS theory of recombination was adapted by Quinlan et al. [43] to the case where quasiparticle-pair energy is converted to antiferromagnetic spin fluctuations, rather than phonons. As we explain below, the results of this calculation cannot be compared directly with β. The recombination rate at low T is predicted to vary as T^3. Therefore γ_{th} is not proportional to n_{th}, which, as we have seen, varies as T^2. Expressed in the language of this thesis, β vanishes in the limit that T goes to zero, in contrast to the T-independent value observed experimentally.

The prediction that $\gamma \propto T^3$ while $n_{th} \propto T^2$ is a reflection of the underlying Fermi liquid theory (FLT). In FLT the normal state scattering rate varies as T^2, while the thermal quasiparticle density varies as T. The corresponding quantities vary as one higher power of T for the d-wave superconductor because its density of states is linear in energy, rather than contant. Thus it is a general consequence of the phase space of Fermi liquids that the quasiparticle scattering rate is not simply proportional the quasiparticle density.

It is interesting, and perhaps relevant, to recall here the celebrated fact that the high-T_c cuprates violate this central prediction of FLT. That is to say, the normal state scat-

tering rate varies linearly, rather than quadratically, with the temperature. In this marginal Fermi liquid (MFL) [50], the scattering rate $\sim 2k_BT/\hbar$ *is* proportional to the quasiparticle density $N(0)k_BT$. The coefficient of proportionality, or β_{MFL}, is simply $\hbar/\pi m^*$. Evaluating this expression with $m^* = 3m_0$ yields β_{MFL}=0.1 cm^2/s, which is remarkably close to the experimental value. This agreement suggests that there may be a close connection between the quasiparticle scattering in the normal state and the antinodal quasiparticle recombination in the superconducting state.

3.5.4 Absence of phonon bottleneck

In the previous section we described two mechanisms for quasiparticle pair recombination. In the more familiar one, the pair is destroyed with simultaneous creation of a 2Δ phonon. In the second mechanism the pair is converted to an electronic excitation, such as an antiferromagnetic fluctuation. Both mechanisms can provide an explanation for the absence of a bottleneck. In the second mechanism, the quasiparticle pair decays to other particle-hole excitations. If the number of particles generated in the pair-destruction process is two or more, then it is highly unlikely for the reverse process to occur. The low rate for the reverse process leads to the absence of a bottleneck.

On the other hand, phonon-mediated recombination is inherently susceptible to a bottleneck because only one particle (the phonon) is created when the pair is destroyed. Previously, we suggested that there are two parameter regimes in which the bottleneck would be avoided; $\gamma_{pc} \ll \beta N(0)\Delta$ or $\gamma_{pc} \ll \gamma_{esc}$. The absence of a bottleneck in the latter case is supported by an analytical solution, provided by Gray [20], of the RT equations in the linear regime ($n_{ph} \ll n_{th}$). At low temperatures, where we may expect $\gamma_{th} \ll \gamma_{pc}$, the

excess quasiparticle population decays with lifetime $\tau \approx (1+\gamma_{pc}/\gamma_{esc})/2\gamma_{th}$. The analytical solution shows that τ is a direct measure of γ_{th}, when $\gamma_{pc}/\gamma_{esc} \to 0$.

The RT equations have not been solved analytically in the nonlinear regime where $n_{ph} \gg n_{th}$. However, we can use general arguments to quantify the conditions necessary for decay of the excited population to reflect the underlying quasiparticle recombination rate. First we analyze the case where $\gamma_{pc} \ll \beta N(0)\Delta$. Following pulsed injection, the bottleneck sets in when the pair destruction and creation rates become equal, or $\beta n_{ss}^2 = 2\gamma_{pc}N_{ss}$, where n_{ss} and N_{ss} are the quasiequilibrium steady-state densities of quasiparticles and 2Δ phonons, respectively. The size of n_{ss} relative to the initial density n_0 is a measure of the strength of the bottleneck. In the weak bottleneck regime, where n_{ss} is much less than n_0, the density decays to a small fraction of initial value before the onset of quasiequilibrium.

The ratio n_{ss}/n_0 can be calculated using conservation of energy, which implies that $2n_{ss} + N_{ss} = 2n_0$. The result is

$$\frac{n_{ss}}{n_0} = \frac{\lambda}{2}(\sqrt{1+\frac{4}{\lambda}} - 1), \tag{3.11}$$

where $\lambda \equiv 2\gamma_{pc}/\beta n_0$. The weak bottleneck regime corresponds to $\lambda \ll 1$, in which case the steady state density is very small, $n_{ss}/n_0 \approx \lambda^{1/2}$. In the strong bottleneck regime, $\lambda \gg 1$, the steady state density nearly equals the initial density, $n_{ss}/n_0 \approx 1 - 1/\lambda$.

To determine whether the cuprates are in the strong or weak bottleneck regime, we must estimate the magnitude of λ. To do so we first recognize that λ must exceed a λ_{min}, obtained by setting n_0 equal to $N(0)\Delta$, the maximum quasiparticle density in the superconducting state. We can evaluate λ_{min} in the dirty s-wave case, as Kaplan et al.

[30] have calculated γ_{pc} as well as β in this regime. The characteristic phonon decay rate is given by $\gamma_{pc} = 4\pi^2 N(0)\alpha^2\Delta/\hbar N$, where N is the number density of ions. Given this phonon decay rate, we find that

$$\lambda_{min} = \frac{2\pi}{\hbar}\frac{N(0)}{NF(2\Delta)}. \tag{3.12}$$

The simplicity of this result is a consequence of detailed balance in the dirty-limit. Eq. 3.12 shows that the strength of the bottleneck is determined by the ratio of the electron density of states at the Fermi level to the phonon density of states at 2Δ. It is clear that the high-T_c cuprates can be in the weak bottleneck regime, where λ is very small, in contrast with conventional low-T_c superconductors. In the high-T_c materials the gap energy is large, and 2Δ coincides with large phonon density of states peaks associated with optic phonons. Furthermore, the density of states at the Fermi level is small compared with conventional metals. Both factors favor small λ. In contrast, in conventional superconductors phonons with energy 2Δ lie in the low-energy tail of the acoustic spectrum. Therefore the density of resonant phonon states is small. This fact, together with the large electronic density of states, place conventional superconductors in the strong bottleneck regime.

The second regime where the bottleneck is avoided is $\gamma_{pc} \ll \gamma_{esc}$. In this case quasiequilibrium is never achieved because phonons are rapidly removed before they can break pairs. Following pulsed photoexcitation N_{ph}, the nonequilibrium phonon density increases from zero, reaches a maximum, and then decays rapidly. The peak value of N_{ph}, or $N_{ph,max}$, can be estimated by setting $\dot{N} = 0$ in Eq. 3.2. In the limit that $\gamma_{pc} \ll \gamma_{esc}$, this yields $N_{ph,max} = \beta n_{ph}^2/2\gamma_{esc}$. If this value is then substituted back into Eq. 3.1, we see that

the maximum value of the pair creation rate is $\beta n_{ph}^2 \gamma_{pc}/\gamma_{esc}$. This term corresponds to a fractional correction to the decay rate equal to γ_{pc}/γ_{esc}. This mechanism for avoiding the bottleneck is also quite plausible in the cuprate superconductors, where 2Δ phonons have very high energy ≈ 60 meV and therefore may have short lifetimes.

3.6 Summary

The most significant observation reported here is the strong dependence of the decay rate of the transient reflectivity on both temperature and pump laser intensity. At low T the decay rate is a linear function of I. At low I the decay rate decreases exponentially with decreasing T. At the lowest values of T and I probed by our experiments, the lifetime of the photoexcited state becomes extremely long, ≈ 600 ps. There is no indication that the lifetime would not continue to increase if the experiment could access lower values of T and I.

In our analysis of the data, we first addressed the nature of the excitations probed by measuring ΔR. We presented arguments that ΔR is proportional to the density of high-energy or antinodal quasiparticles created by the laser excitation. We explained theoretically why such particles, although not the lowest energy excitations, could be highly metastable at low temperature and density. The metastability is a consequence of the limited phase space for decay of high-energy quasiparticles to the nodal regions of the Brillouin zone. As the phase space restrictions rely on momentum conservation, the degree of metastability may be expected to be highly sensitive to disorder.

Having understood the stability of an isolated quasiparticle, we sought a quantita-

tive understanding of the decay process that occurs when a pair of quasiparticles interact. We estimated the magnitude of the recombination coefficient, β, from both the T and I dependence of the decay rate. We emphasized that β is a direct measure of the strength of quasiparticle interactions. In addressing the theoretical approaches to the recombination rate, we identified $\hbar/m^*$ as the natural unit for β in a two-dimensional superconductor. We pointed out that while recombination is assumed to be phonon-mediated in conventional superconductors, electron-electron mediated processes must be considered as well in the cuprates. In the context of phonon-mediated processes, we discussed the need to extend the work of Kaplan et al. [30] to the 2D, clean limit that is applicable to the cuprates. In the electron-electron mediated case, more work is needed to understand the underlying recombination process. As a motivating factor, we pointed out the remarkable coincidence between the normal state scattering rate and the superconducting state recombination rate. We showed that both processes have the same dependence on the quasiparticle density, which can be described by an interaction coefficient equal to $\hbar/\pi m^*$.

Chapter 4

Doping dependence in BSCCO system

4.1 Introduction

Rapid developments in time-resolved optical spectroscopy have led to renewed interest in the nonequilibrium state of superconductors and other highly correlated electron materials. In these experiments, the nonequilibrium state is prepared by the absorption of short (less than 100 fs) laser pulses, typically in the near-infrared, that perturb the density and energy distribution of quasiparticles. The evolution of the nonequilibrium state is probed by time-resolving the changes in the optical response functions of the medium that take place after photoexcitation. The nonequilibrium state of the cuprate superconductors, in particular, has been studied extensively. Ultimately, the goal of such experiments is to understand not only the nonequilibrium state, but to shed light on the still poorly under-

stood equilibrium properties of these materials. Recently, nonequilibrium experiments have revealed aspects of the cuprates that have been inaccessible by other techniques. For example, both the diffusion and recombination coefficients of quasiparticles have been measured in underdoped single crystals of $YBa_2Cu_3O_{6.5}$ using time-resolved optical spectroscopy.

One obstacle in our attempts to understand the nonequilbrium state of cuprates has been the apparent nonuniversality of some of its properties. Perhaps the most basic property is the time scale for return to equilibrium. In optimally doped $YBa_2Cu_3O_{6.95}$ (YBCO), the first and most thoroughly studied cuprate, this time scale has been measured using terahertz, infrared, and visible probe beams. In all cases the lifetime is very short, roughly 2 ps, and is nearly independent of the initial density of nonequilibrium quasiparticles, n_0, and temperature, T. More recently, it was discovered that in $YBa_2Cu_3O_{6.5}$, an underdoped material with a T_c near 60 K, the lifetime measured at temperatures below 10 K extrapolates to greater than 1 ns in the limit that n_0 goes to zero, almost a factor 10^3 longer than found in optimally doped YBCO under the same excitation conditions.

Another property that varies from one cuprate material to another is the sign of the photoinduced change in reflectivity, ΔR, in the near-infrared regime. The fact that the relaxation rates and the sign of ΔR are nonuniversal has hampered the search for unified understanding of the nonequilibrium state. Here, we report a study of the nonequilibrium state in the $Bi_2Sr_2CaCu_2O_{8+d}$ (BSCCO) system that sheds light on these seemingly disparate results. Our measurements reveal that the nature of the relaxation process in BSCCO superconductors changes drastically, precisely at optimal doping. Further, we find that the sign of ΔR changes at the same hole concentration at which the sudden change

in dynamics takes place. Our results raise the possibility that the disparities in relaxation rate and sign of ΔR observed in other cuprate samples may be a consequence of a general, or perhaps universal, change in quasiparticle dynamics that takes place at optimal doping.

4.2 Experimental results

Time-resolved optical spectroscopy was performed using pump and probe pulses of photon energy 1.5 eV and duration 80 fs derived from a mode-locked Ti:Sapphire. The samples are single crystals of $Bi_2Sr_2CaCu_2O_{8+d}$ with T_c's ranging from underdoped 39 K to overdoped 72 K. The single crystals of BSCCO are grown with a floating zone method and are carefully annealed and quenched to obtain uniform oxygen content inside the sample [1].

Because the BSCCO crystals are optically thick at the laser wavelength of 820 nm, the changes in optical response were probed by measuring the reflected probe intensity. Preliminary measurements on these samples revealed that the average power of the pump pulses caused an unacceptable level of heating. Such effects, not encountered in YBCO, can be traced to the much lower thermal conductivity of BSCCO, particularly in the c-axis direction. In order to study the nonequilibrium state at low temperature, we inserted an acousto-optic pulse-picker at the laser output. The pulse picker was configured to direct only 1 in N pulses to the sample, where N=18, 36, etc. The data presented here were collected with N=18, reducing the 90 MHz pulse repetition rate of the laser to 5 MHz. At this rate the indications of heating were absent, and further reduction to 2.5 MHz produced no additional changes in the amplitude or decay rate of ΔR. Fig. 4.1 is a plot of the

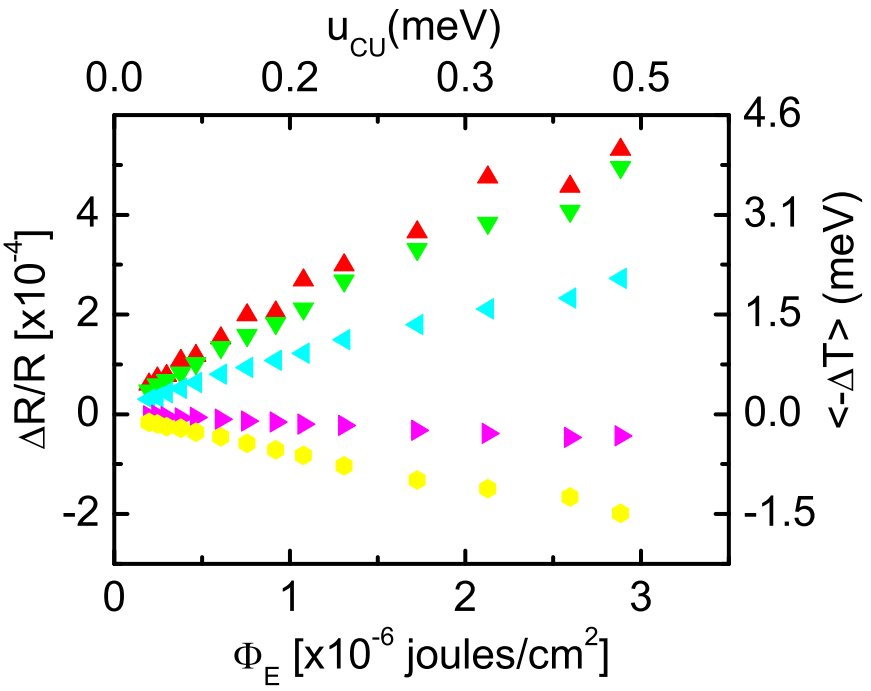

Figure 4.1: The reflectivity change, ΔR, normalized to the reflectivity R, as a function of the energy per area, Φ_E, deposited by each pump pulse. The data shown is for samples with (top to bottom) 70 K (underdoped), 79 K, 90 K (underdoped) 93.5 K (optimal) and 72 K (overdoped).

reflectivity change, ΔR, normalized to the reflectivity R, as a function of the energy per area, Φ_E, deposited by each pump pulse. The data shown were obtained from a series of BSCCO crystals whose T_c's range from 70 K (underdoped) to 72 K (overdoped). The plot shows ΔR measured at 0.2 ps delay, before the decay of the reflectivity change has begun. For each of the samples ΔR increases linearly at low Φ_E, and shows some indication of saturation at high Φ_E in the underdoped samples. The most striking feature of the data is the change in sign of ΔR, which takes place between the Tc=90 K (underdoped) and Tc=93.5 K (optimally doped) samples.

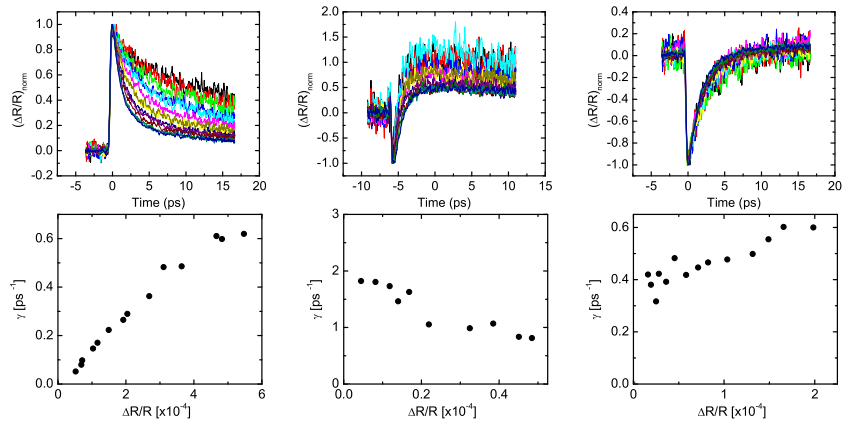

Figure 4.2: Normalized reflectivity change *vs.* time (top panel) and the initial decay rate γ_0 *vs.* initial reflectivity change, $\Delta R/R$ (bottom panel at 5K for three samples with T_c's left to right 70 K (underdoped), 93.5 (optimal) and 72 K (overdoped). Different colors in the top panel are different laser intensities, slower curves being the low intensity and faster curves being the high laser intensity.

Fig. 4.2 illustrates the crossover in quasiparticle dynamics that takes place at the same hole concentration at which ΔR changes sign. Here we present results for three representative samples: underdoped (Tc=70 K), optimally-doped (Tc=93.5 K), and overdoped (Tc=72 K). The top panels show $\Delta R/R$ as a function of time delay after absorption of the pump pulse, for different values of the pump laser fluence. As shown previously, the maximum $\Delta R/R$ increases approximately linearly with Φ_E. In order to compare the decay rates at different Φ_E, we scaled the amplitude to the same value near time-delay zero. For each sample the graph appearing below the decay curves is a plot of the initial decay rate, γ_0, of $\Delta R/R$ as a function of Φ_E.

The representative samples show that two basic features of $\Delta R/R$ change character at optimal doping. The first feature is the sign, which has already been shown to

change from positive to negative in Fig. 4.1. The second feature is the dependence of the decay rate on excitation density. In the underdoped sample the decay becomes slower with decreasing Φ_E. The lower panel shows that the dependence of γ_0 on Φ_E is linear, with essentially zero intercept (we estimate an experimental uncertainty in γ_0 of 0.005 ps^{-1}, which is approximately 10^{-2} of the maximum γ_0 of 0.7 ps^{-1}). Thus, in the underdoped sample the lifetime of the excitations created by the laser appears to diverge as their initial density tends to zero.

The two adjacent panels show that the dynamics of photoexcitations in the optimal and overdoped samples are substantially different. Focusing first on the overdoped sample, the sign change of ΔR is accompanied by a pronounced change in the relaxation dynamics. The decay rate of the excited state is now essentially independent of the initial excitation density. In the optimal sample the decay of ΔR appears at first to be complicated, showing a sign reversal and some dependence on the excitation density. Considered in isolation the curves would be difficult to interpret. However, recognizing that the optimally doped sample sits precisely at a crossover in both the sign of ΔR and its relaxation dynamics helps considerably in interpreting these curves. In fact, each of the curves can be modelled as a superposition of two responses, one positive and dependent on Φ_E, the other negative and independent of Φ_E. Figs. 4.3(a) and 4.3(b) summarize the data for each of the samples used in this study, showing the crossovers in the amplitude and decay rate of ΔR. Fig. 4.3(a) is a plot of ΔR measured near zero time delay as a function of hole concentration x, for different values of the laser intensity. Fig. 4.3(b) shows γ_0 vs. x, again for different values of Φ_E. The values of x were obtained from the transition temperatures using the

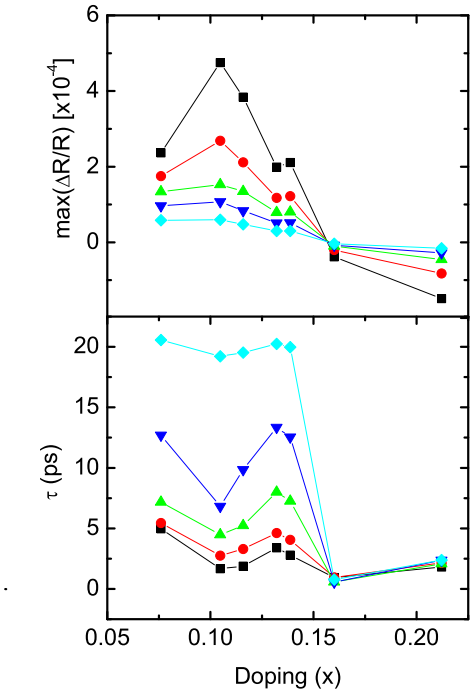

Figure 4.3: (a) Amplitude of $\Delta R/R$ *vs.* doping (x). (b) Initial decay rate (γ_0) of $\Delta R/R$ *vs.* doping (x). Different colors are different laser intensities.

empirical formula, $x(T_c) = 0.16 \pm [(1/82.6)(1 - T_c/T_c^{max})]^{1/2}$ [28]. The sharpness of the crossover is shown most clearly in the behavior of γ_0 at the lowest Φ_E. For underdoped samples, γ_0 becomes very small at low Φ_E. However, at optimal doping and above, where γ_0 is Φ_E-independent, the rate becomes suddenly greater by more than a factor of ten.

While coincidence cannot be ruled out, our results suggest the possibility of a connection between the sign of ΔR and quasiparticle relaxation. In the following, we discuss the hole-concentration dependence of these two features, starting with the sign of ΔR. We conclude with speculation regarding the possible connection between these two aspects of the nonequilibrium state.

4.3 Discussion

We first consider how the presence of nonequilibrium excitations affects the dielectric function, ε. In general, the occupation of excited states can only shift optical spectral weight from one frequency range to another, because the total spectral weight is conserved. The change in dielectric function, $\delta\varepsilon$, that results from this shift depends on the relative ordering of the measurement frequency, ω_0, and frequencies where spectral weight is lost and gained. In the BCS picture, the generation of nonequilibrium quasiparticles shifts spectral weight from the condensate d-function at $\omega = 0$ to a narrow Drude peak. If the system is probed at a much higher frequency, then $\Delta\varepsilon_1$ at ω_0 is given by [45],

$$\Delta\varepsilon_1 \cong -\frac{8}{\omega_0^4}\int d\omega \Delta\sigma_1(\omega)\omega^2 \tag{4.1}$$

The corresponding change in reflectivity, ΔR, can be calculated from the Fresnel equation. Using literature values for the dielectric function of the BSCCO system at 1.5 eV, we find that $R^{-1}\partial R/\partial\varepsilon_1 = 0.02$. Thus the mechanism described in Eq. 4.1 can only produce a negative ΔR and cannot account for the photoinduced response in underdoped BSCCO.

In order for nonequilibrium excitations to increase ε_1, their presence must shift low frequency spectral weight to a frequency much higher than ω_0, in which case $\Delta\varepsilon_1 \cong 8A/\omega_0^2$, where A is the area under $\Delta\sigma_1(\omega)$. Such a spectral weight transfer, which is clearly outside the realm of BCS theory, was suggested to account for recent observations of thermal changes in ε_1 measured near 1 eV in BSCCO [39]. It was reported that ε_1, and consequently R, increase with heating through the superconducting transition temperature. The sign of this effect is consistent with the photoinduced changes in underdoped BSCCO that we measure,

in that for both cases R increases with a weakening of superconductivity.

In discussing their results, Molegraaf et al. used the Maldague theorem to equate spectral weight shift to change in kinetic energy of the conduction electrons. In order to compare the photoinduced and thermally induced change in ε_1, we convert our measured ΔR to kinetic energy change using the relation, $A = (e^2/\hbar^2 d)\langle -\Delta T\rangle$, where d is the spacing between the conducting Cu-O planes. We use the resulting conversion factor, $\langle -\Delta T\rangle = (7.6eV)\Delta R/R$, to add a scale of energy to the (right-hand side) vertical axis of Fig. 4.1. We see that according to this interpretation, weakening superconductivity through photoexcitation leads to changes in kinetic energy per electron on the scale of couple of meV. This is comparable to the change found when superconductivity is weakened thermally.

Further insight into this mechanism is gained by converting the horizontal axis as well, from energy deposited per area to energy deposited per Cu plaquette, u_{Cu}. We use the conversion, $u_{Cu} = a_{Cu}\Phi_E d/\delta$, where a_{Cu} is the plaquette area and d is the penetration depth of the laser energy. We note that the energy deposited per plaquette is on the scale of tenths of meV.

Within this interpretation, the sign of ΔR in the underdoped BSCCO samples indicates a reduction in kinetic energy in the superconducting as compared with normal state. The sign is consistent with that inferred from the thermally-induced changes in $varepsilon_1$. However, within the same interpretation, the kinetic energy increases in the superconducting for the overdoped sample. This increase in kinetic energy agrees with the predictions of the BCS theory, where the transition is driven by potential energy lowering.

Overall, the data are consistent with a crossover from unconventional, kinetic energy-driven superconductivity to potential-energy driven superconductivity at optimal doping.

We turn next to a discussion of the relaxation dynamics of the nonequilibrium state in BSCCO, beginning with the underdoped side of the phase diagram. The linear dependence of γ_0 on Φ_E seen in Fig. 4.2 can be viewed as a consequence of the pairing theory of superconductivity. To reenter the condensate a nonequilibrium quasiparticle must find another to reform a Cooper pair. The rate of such encounters depends linearly on their density. However, it is important to recognize that when two quasiparticles scatter into the condensate they emit an excitation whose energy is equal to the combined energy of the original quasiparticles. Furthermore, the measurement time scale is too short for the energy that is emitted to propagate outside of the volume that is probed optically. Therefore, the decay of ΔR must be interpreted as the conversion of energy from a form which changes the optical response at 1.5 eV, that is nonequilibrium quasiparticles, to one that does not. Identifying the nature of this 'dark energy,' for example vibrational or magnetic, would be a major step towards understanding the mechanism of superconductivity in the cuprates.

With the underdoped response as context, the implication of the crossover to excitation-density independent dynamics is reasonably clear. At optimal doping a new channel for the relaxation of a quasiparticle opens, one that does not involve recombination with another quasiparticle. Such a channel is inelastic scattering, a process in which a single quasiparticle loses energy and momentum and emerges in a final state different from its initial one. The Feynman diagrams for the recombination and inelastic scattering are shown in Fig. 4.4. The quantum of energy emitted in both processes is labelled X, as it is

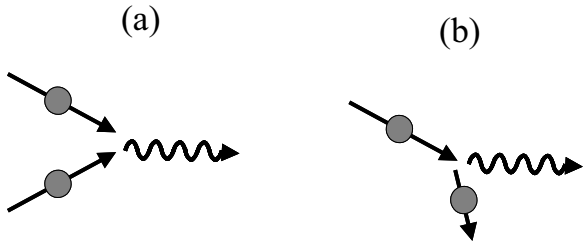

Figure 4.4: The Feynman diagrams for the recombination (a) and inelastic scattering (b).

yet to be identified. The diagrams are closely related, as the two processes have the same excitations entering or leaving the vertex. They differ in that a quasiparticle in the initial state of the recombination process appears in the final state for inelastic scattering. The extra quasiparticle in the initial state causes recombination to depend strongly on excitation density and temperature, whereas scattering is essentially independent of both. In order for scattering to cause ΔR to decay the quasiparticle that appears in the final state cannot itself induce a change in reflectivity at 1.5 eV.

The opening of a channel for quasiparticle scattering suggests a change in the ordering of excited state energies. In fact, it is known from inelastic neutron scattering (INS) and ARPES that a level crossing does indeed take place at optimal doping [13]. ARPES shows that the maximum value of the gap, Δ_M, decreases roughly linearly as a function of x. INS has demonstrated the existence of a spin 1 (triplet) exciton whose energy varies in proportion to T_c as x is varied. On the underdoped side of the phase diagram, Δ_M is larger than the exciton energy, Ω_X. With increasing x, Δ_M decreases while Ω_X increases, and they reach the same value of about 40 meV at optimal doping. Beyond optimal doping the two levels both decrease in energy and remain less that approximately 10 meV apart.

The existence of this level crossing can potentially account for a sudden change

in quasiparticle relaxation, as in the following scenario. Very rapidly after photoexcitation nonequilibrium quasiparticles relax to states near the M point, the antinodal regions of the Brillouin zone. Further relaxation along the Fermi contour towards the node by emission of low energy electron-hole pairs is extremely slow because of energy and momentum conservation. However, emission of a magnetic exciton can occur because it has a very large spread in momentum. Evidence for emission of magnetic excitons by antinodal quasiparticles is seen in the quasiparticle self-energy as measured by ARPES and optical conductivity.

We consider how antinodal quasiparticle relaxation would vary with x in this scenario. For $x < x_{opt}$, relaxation by magnetic exciton emission stops when the quasiparticle energy falls to Ω_X. Once this energy is reached, an isolated quasiparticle is essentially metastable and must find another in order to recombine. At almost precisely optimal doping a channel opens in which an antinodal quasiparticle scatters directly to the nodal region by exciton emission. For $x > x_{opt}$, this channel stays open as because Ω_X and Δ_M remain comparable.

For internal consistency, this scenario requires that nodal quasiparticles emitted in the scattering process do not contribute to the change in R at 1.5 eV. This condition is reasonable, based on our previous discussion of how ΔR originates from shifts of optical spectral weight. Hosseini et al. [26] have demonstrated, using broadband microwave spectroscopy, that the entire spectral weight removed from the condensate by thermal excitation of nodal quasiparticles is transferred to a narrow Drude peak centered on $\omega = 0$. From Eq. 4.1 it follows that De1 due to this spectral weight shift is negligible on the scale of our observations. On more qualitative grounds, it is reasonable to suppose that nodal

quasiparticles weaken superconductivity less than antinodal ones, as their presence does not block the formation of tightly bound Cooper pairs.

We now return to the issue of the coincidence of crossovers at x_{opt} in the sign and relaxation dynamics of ΔR. The notion that the nature of the transition to superconductivity might change at, or near, optimal doping was advanced early in the theoretical study of cuprate superconductivity. Many subsequent experiments, which revealed a pseudogap in the normal state that closes near optimal doping, support this prediction. Thus a crossover in sign of ΔR may be considered as intrinsic to the basic physics of cuprate superconductivity. On the other hand, the degeneracy of the antinodal quasiparticle and the triplet exciton that we have invoked to explain the crossover in dynamics at optimal doping is widely regarded as accidental. However, our data show that the sign and relaxation dynamics are one-to-one correlated, suggesting that the degeneracy may not be accidental.

We conclude with a comment regarding the relation of nonequilibrium experiments to the search for the high-Tc mechanism, which has proved so difficult. Identifying the excitations released when antinodal quasiparticles recombine or inelastically scatter would constitute a breakthrough in this search. These excitations are produced copiously in the nonequilibrium state prepared by absorption of a laser pulse. Developing time-resolved probes that can detect and identify these excitations may be a fruitful strategy for uncovering the basis of cuprate superconductivity.

Chapter 5

Transient Grating Spectroscopy

The transient grating technique has been used successfully in a wide variety of applications, including exciton diffusion, dynamics of biomolecules, propagation of ultrasound, and thermal diffusion [12]. In this technique, a pair of laser beams is interfered on a sample, producing a sinusoidally varying pattern of intensity, and hence photoexcitation density. If the presence of photoexcitations affects the index of refraction of the material, the interfering pump beams create a diffraction grating at the sample surface. The time evolution of this transient grating provides information about the relaxation and propagation of excitations created by the laser beams.

In this chapter, we will describe the phase matching condition, heterodyne detection, phase calibration and experimental implementation of the transient grating.

5.1 The basics of the transient grating

To probe the time evolution of the grating, a third beam is sent onto the sample. The probe is specularly reflected (or transmitted in the case of an optically thin sample) and diffracted from the transient grating. The direction of the diffracted beam is determined by conserving energy and momentum parallel to the plane of the sample. Momentum perpendicular to the plane is not conserved.

One way to think about the physical process in transient grating experiment is to consider absorption of one of the two pump beam photon and a probe beam photon and simultaneous emission of the other pump beam photon and a diffracted beam photon. If the two pump beams that create the grating have the wave vectors $\mathbf{k_1}$ and $\mathbf{k_2}$, and the probe beam and the diffracted beam have wave vectors $\mathbf{k_p}$ and $\mathbf{k_s}$, then this process would be simultaneous absorption of $\mathbf{k_1}$ and $\mathbf{k_p}$ together with simultaneous emission of $\mathbf{k_2}$ and $\mathbf{k_s}$. In a degenerate transient grating experiment, energy conservation dictates that $|\mathbf{k_1}| = |\mathbf{k_2}| = |\mathbf{k_p}| = |\mathbf{k_s}| = k$. Since the momentum parallel to the sample plane is conserved, then $k_1^{||} + k_p^{||} = k_2^{||} + k_s^{||}$. By symmetry, we can also consider absorption of $\mathbf{k_2}$ and $\mathbf{k_p}$ photons with emission of $\mathbf{k_1}$ and $\mathbf{k_s}$. In this case, $k_2^{||} + k_p^{||} = k_1^{||} + k_s^{||}$. Therefore, in general there would be two different different diffracted beams corresponding to ± 1 diffraction orders with $(k_s^{\pm})^{||} = k_p^{||} \pm q^{||}$ where $\mathbf{q} = \mathbf{k_1} - \mathbf{k_2}$ and $|\mathbf{k_s^{\pm}}| = k$.

To better visualize the momentum and energy conservation, Fig. 5.1 (a) illustrates two dimensional problem where two pump beams with wave vectors $\mathbf{k_1}$ and $\mathbf{k_2}$ and wavelength λ are incident on the sample each making an angle θ with the sample normal. Interference of these two beams creates an intensity grating with wavelength $\lambda_g = \lambda/(2sin\theta)$

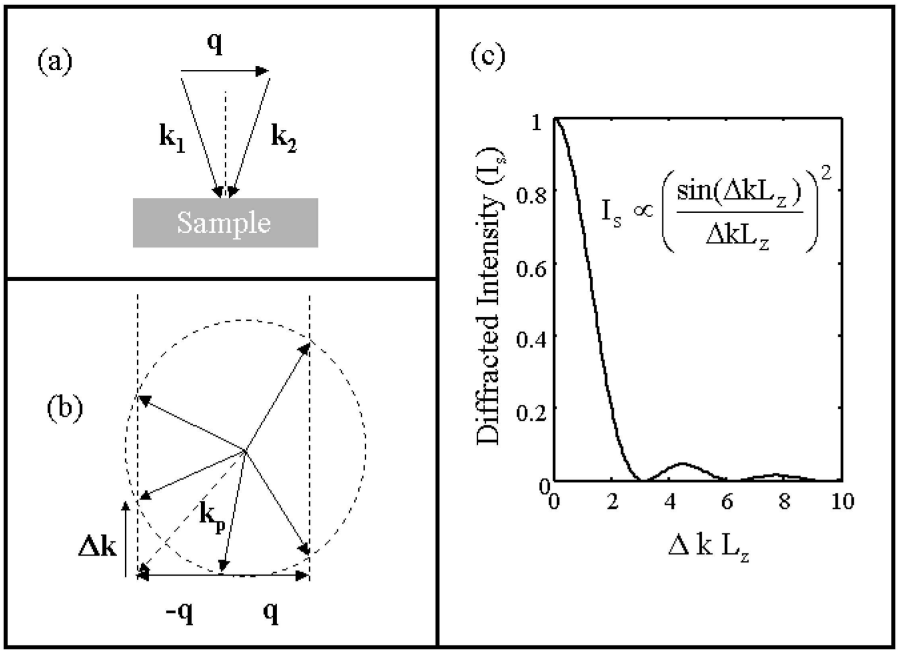

Figure 5.1: Geometry of the transient grating experiment. (a) Two pump beams ($\mathbf{k_1}$ and $\mathbf{k_2}$ with $\mathbf{q} = \mathbf{k_1} - \mathbf{k_2}$) symmetrically incident on the sample create the grating. (b)Probe beam $\mathbf{k_p}$ is diffracted off of the grating according to energy conservation and momentum conservation in the plane of the sample. Both forward (transmitted) and backward (reflected) diffracted wave vectors for the ± 1 diffraction orders are shown (a total of four wave vectors). Δk is the mismatch in the momentum in the direction perpendicular to the sample surface. (c)The intensity of the diffracted wave (I_s in arbitrary units)is plotted as a function of $\Delta k L_z$ for a fixed value of L_z where L_z is the thickness of the grating. For a fixed value of L_z, diffraction intensity is maximum for $\Delta k = 0$, known as the phase-matching condition.

and wave vector ($\mathbf{q} = \mathbf{k_1} - \mathbf{k_2}$) parallel to the sample surface. In Fig. 5.1 (b) a probe beam incident on the sample with a wave vector $\mathbf{k_p}$ is diffracted into four possible wave vectors, corresponding to the ± 1 orders of the transmitted and reflected diffracted waves. These wave vectors are obtained by conserving energy and momentum in the plane of the sample. Dashed circle in the figure has a radius of k. Conservation of the energy is managed by having the tip of every wave vector to lie on the circle. To conserve the total momentum, $\mathbf{k_p}$ can change by $\pm\mathbf{q}$. But in general, the resulting wave vectors $\mathbf{k_p} \pm \mathbf{q}$ will not lie on

the circle. But since only momentum parallel to the sample surface is conserved, the wave vectors for the diffracted waves will have the same parallel momentum component as $\mathbf{k_p} \pm \mathbf{q}$ and lie on the circle. Geometrically, this is obtained by drawing perpendicular lines at the tips of $\mathbf{k_p} \pm \mathbf{q}$. The points where these lines (shown as dashed lines in Fig. 5.1 (b)) intersect the circle correspond to wave vectors for which energy and momentum in the plane is conserved.

Fig. 5.1 (b) also shows the mismatch in the momentum perpendicular to the surface (Δk) for one of the diffraction orders. The intensity of the diffracted signal (I_s) depends on Δk and the grating thickness (L_z). L_z is determined by the length of the interaction region of the beams inside the sample. For a fixed value of L_z, $I_s \propto [sin(\Delta k L_z)/(\Delta k L_z)]^2$ [25]. Fig 5.1 (c) shows a plot of the I_s as a function of $\Delta k L_z$ for a fixed value of L_z. Maximum diffracted intensity is obtained for a perfect phase-matched geometry i.e. when $\Delta k = 0$. Therefore, it is desirable to have $\Delta k = 0$ for maximum diffraction efficiency.

5.2 "Boxcar" phase matching geometry

To maximize the diffracted intensity, we need to satisfy the phase matching condition. In three dimensions, two beams and the probe beam can be arranged to satisfy this condition. A very common geometry used for this is known as the "boxcar" geometry [35]. A simple drawing of this geometry is shown in Fig. 5.2. Three parallel beams, pump 1, pump 2 and probe are arranged parallel to each other so that the laser spots form the three corners of a rectangle in a plane perpendicular to their path. A lens with axis passing through the center of this rectangle is used to focus the beams onto the sample under study.

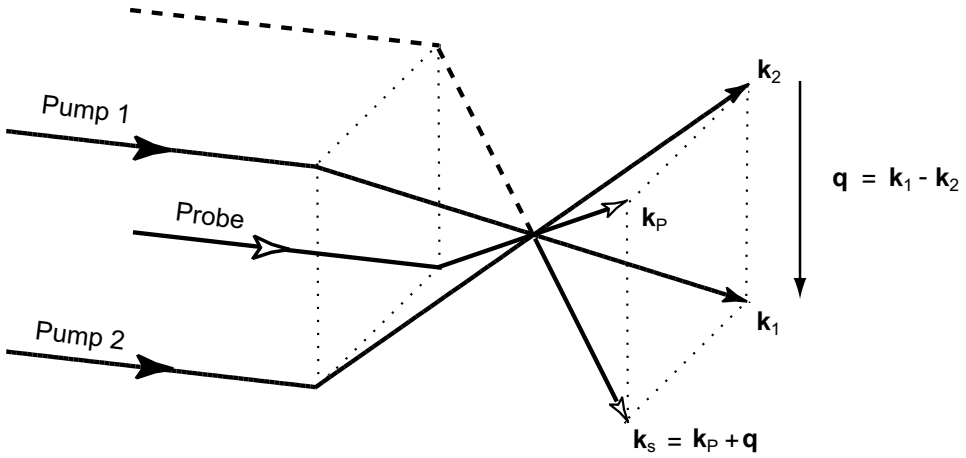

Figure 5.2: "Boxcar" phase matching geometry of the transient grating experiment. Three parallel beams, pump 1, pump 2 and probe are arranged parallel to each other so that the laser spots form the three corners of a rectangle in a plane perpendicular to their path. A lens with axis passing through the center of this rectangle is used to focus the beams onto the sample under study. Diffracted beam emerges along the fourth corner of the rectangle since $\mathbf{k}_s = \mathbf{k}_p + \mathbf{q}$ where $\mathbf{q} = \mathbf{k}_1 - \mathbf{k}_2$.

Diffracted beam with wave vector $\mathbf{k}_s$ will emerge through the fourth corner of the rectangle, since $\mathbf{k}_s = \mathbf{k}_p + \mathbf{q}$ where $\mathbf{q} = \mathbf{k}_1 - \mathbf{k}_2$.

This arrangements of the beams automatically satisfies the energy conservation and the momentum conservation. Also, it is convenient because it provides a way of knowing the direction of diffracted beam. Since the signal is typically weak, it is often very helpful to know the direction before the experiment.

Up to know, we have discussed the creation of the grating, phase matching condition and the "boxcar" geometry of the transient grating. In the following section, we will discuss the experimental implementation of transient grating technique.

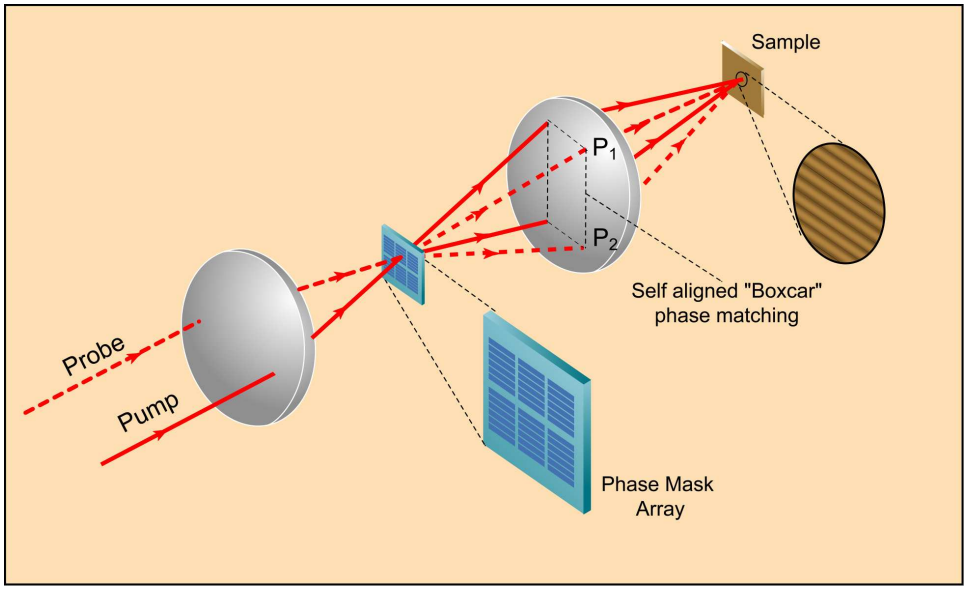

Figure 5.3: Experimental setup for complete characterization of a transient grating in reflection geometry. For clarity only incident pump and probe beams are shown.

5.3 Transient grating setup

In this section, we describe an experimental setup capable of complete transient grating characterization in a reflection geometry. This setup is built on the pump probe setup described in Fig. 2.1. The part of pump probe setup in Fig. 2.1 before the lens is exactly same in the transient grating setup. All the optics for the transient grating are placed after this lens. Here we will only describe the part of the setup after the lens, since prior to the lens it is already described in Chapter 2.

Fig. 5.3 shows the transient grating setup. A transmission grating (phase mask) is placed in the focus of the pump and probe beams instead of the sample in Fig. 2.1. Both pump and probe beams are split into two identical replicas using this phase mask [19, 38]. A spherical mirror and a plane folding mirror (represented schematically by the second lens in the sketch) focus the beams onto the sample. The spherical mirror is placed such that

the phase mask is at the center of the mirror. It is rotated couple of degrees to get the beams on to the folding mirror which focuses them on to the sample. In Fig. 5.3, we only show the incident beams, the path of the reflected beams will be discussed below.

5.3.1 The use of diffractive optics

The most important part of the transient grating setup is the use of a phase mask to split the beams. Phase masks are surface relief gratings etched in fused silica. There are several reasons to use a phase mask rather than a regular beam splitter [18]. The advantages are (1) automatic beam alignment for "Boxcar" phase matching as shown with a dashed rectangle in Fig. 5.3; (2) automatic spatial and temporal overlap of the signal and reference beams on the detector; (3) tilted wavefronts which preserves the temporal and spatial resolution between the object and image plane contrary to a regular beam splitter; (4) high efficiency comparable to regular beam splitters; (5) passive phase stability between the input fields which eliminates the need for active phase locking.

We used a custom made phase mask manufactured by Digital Optics Cooperation optimized for 800 nm. It consists of 10 different phase mask etched in a square shape (2.5 mm by 2.5 mm) on fused silica substrate. They have periods ranging from 2 μ to 10 μ. Since the grating formed on the sample has half the period as the phase mask, in theory we can generate gratings with periods ranging from 1 μ to 5 μ. In practice, this is limited by the f number of the spherical mirror. Lower grating periods require higher incidence angles, therefore high f numbers. Our spherical mirror had a radius of 12" and an aperture diameter of 6", so we can go down to 2 μ gratings rather than 1 μ. This can be improved simply by putting in a higher f number spherical mirror.

The phase mask is mounted on a XYZ translational stage which allows switching between the different gratings without changing the alignment. As will be explained below, reflected beams also return back through the same phase mask. Therefore the only thing we need to do to change the grating period is to translate the phase mask, everything else stays unchanged and the setup is self aligned for all the gratings. This provides the ability to change the grating period in just couple seconds.

To create the grating two pump beams are required, but in principle one probe beam is enough to probe the grating. When using a diffractive optics, two probe beams are generated labelled as P1 and P2 in the Fig. 2.1. One can either block one of them and do "homodyne" detection or use both beams to do "heterodyne" detection. In the following section, we will describe and compare the two different detection techniques.

5.4 Homodyne and Heterodyne detection of the grating

The intensity of the diffracted beam depends quadratically on the amplitude of the index change, δn. Because δn is often very small, the diffracted signal can be difficult to measure using standard methods of intensity (or homodyne) detection. Moreover, since photo-detection of intensity destroys information about the phase, it is not possible to measure the real and imaginary parts of δn. This is a significant limitation, because information about the complex phase angle of δn is often useful in constructing a physical model of the photo-excitation process.

Heterodyne detection is an alternative detection method that enhances sensitivity and preserves the phase information contained in the diffracted probe beam [51, 6]. In this

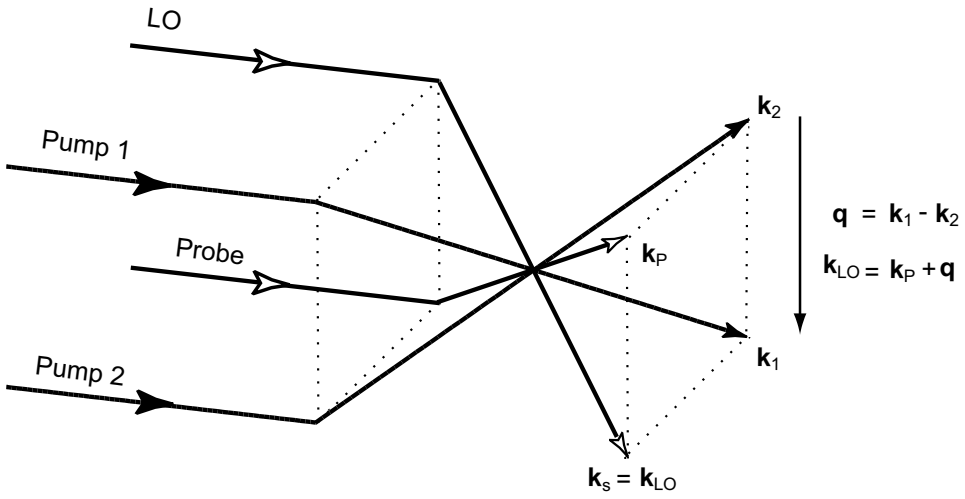

Figure 5.4: Heterodyne detection in the "Boxcar" phase matching geometry of the transient grating experiment. The pump beams that create the grating are incident along $\mathbf{k}_1$ and $\mathbf{k}_2$ and the probe and LO beams are incident along $\mathbf{k}_P$ and $\mathbf{k}_{LO}$. Since $\mathbf{k}_{LO} = \mathbf{k}_P + \mathbf{q}$, diffracted probe beam emerges collinear with the specular or transmitted LO.

technique, the probe is mixed with another beam from the same laser which acts as a local oscillator (LO). "Boxcar" geometry explained in Section 5.2 can be used to implement self aligned heterodyne detection. In Fig. 5.2, if we send the LO beam along the fourth corner of the rectangle then it is guaranteed that the diffracted signal will be collinear with this beam. This is shown in Fig. 5.4.

In a typical experiment, the beam containing both the diffracted probe and LO are directed to a standard photodetector. The output current of the detector (I_D) is related to the total intensity,

$$I_D \propto |E_{LO}|^2 + |E_S|^2 + 2Re(E_{LO}E_S^*) \tag{5.1}$$

where E_{LO}, and E_S are the electric field of the LO and diffracted probe respectively. The last term on the right-hand side of Eq. 5.1 corresponds to the mixing of the LO and the signal carrying beams.

We can see the improvement in the signal amplitude by analyzing the terms on the right hand side in more detail. The first term is independent of δn. The second term is the homodyne signal, which is second order in δn. The third term is the heterodyne signal and is linearly proportional to δn. In many experiments $\delta n \approx 10^{-4} - 10^{-5}$, and the third term is four to five orders of magnitude larger than the second term. In this range of δn, heterodyne detection can provide four to five orders of magnitude improvement in signal as compared with conventional homodyne detection.

The mixing term in Eq. 5.1 can be expressed in the form $2E_{LO}E_S \cos\phi$, where ϕ is the phase of the signal relative to the LO. This phase can be varied by changing the relative optical path length of the probe and LO beams. In practice, a convenient method to achieve a continuous scan of ϕ is to pass one of the beams through a thin glass coverslip placed on a rotating mount. Measuring the detector current as a function of the coverslip angle yields a direct measurement of ϕ for any position of the coverslip.

5.5 Phase calibration

A problem encountered in transient grating experiments is that it is difficult to determine the complex phase angle of δn from a measurement of ϕ. As will be shown below, ϕ can be written as $\phi = \phi_S + \phi_{12} - \phi_{LP}$ [19] where ϕ_{12} is the relative phase of the two pumps, ϕ_{LP} is the relative phase of the LO and probe before interacting with the sample, and ϕ_S is the phase shift caused by diffraction from the transient grating. The latter quantity is directly related to the phase of δn. It is clear from the expression above that determining ϕ_S requires knowledge of ϕ_{12} and ϕ_{LP}, which are difficult to measure. Prior to this work

the usual approach has been to calibrate the system by using a reference material, in which the phase of δn is known [19, 38].

This method of phase calibration has several limitations. First, any uncertainty in the response of the reference sample introduces a systematic error in the measurements. Second, this method is incompatible with measurements performed in a reflection geometry, as the position and orientation of the sample and reference must be kept the same to a high degree of accuracy. Finally, the calibration must be performed frequently to compensate for phase drifts due to temperature variation and other environmental effects.

In this section, we introduce a new method that provides a far more convenient and accurate phase calibration. It eliminates the need for a reference sample and can be used both in reflection and transmission geometries. Our method is based on the symmetry between the LO and the probe beams. In the phase-matched boxcar geometry, the probe beam and the LO are interchangeable. Each beam is diffracted into the specular beam of the other. Since the two beams are symmetrical in this sense we will refer to them as P1 and P2, rather than probe and LO. As we show below, comparing the photodetector current as a function of ϕ (or coverslip angle) when P1 is the LO with that obtained when P2 is the LO provides the extra information required for absolute phase calibration.

The fields of the pump beams that create the grating can be written as the real parts of the complex fields $E_1 = Ee^{i(\mathbf{k}_1 \cdot \mathbf{r} + \phi_1)}$ and $E_2 = Ee^{i(\mathbf{k}_2 \cdot \mathbf{r} + \phi_2)}$. The intensity at the sample surface produced by the superposition of these fields is proportional to $|E|^2[1 + cos(qx + \phi_{12})]$ where $\mathbf{q} = q\hat{\mathbf{x}}$ and $\phi_{12} = \phi_1 - \phi_2$. (In order to focus on the absolute phase calibration, we treat the limit where the grating thickness is much smaller than the

wavelength. In this case the grating must be probed in a reflection geometry. The extension to the thick grating case and transmission geometry is straightforward). Assuming that the photoinduced change in reflection coefficient (δr) is proportional to the local light intensity, the reflection coefficient at the surface immediately after photoexcitation is given by $r = r_0 + \delta r[1 + cos(qx + \phi_{12})]$ where r_0 is the equilibrium reflectivity. For times after photoexcitation the reflectivity can be written in the form $r(t) = r_0 + \delta r(t)[1 + \varepsilon(t)cos(qx + \phi_{12})]$ where ε is the ratio of the grating amplitude to its mean value.

As stated previously, each probe beam is both diffracted and specularly reflected from the reflectivity grating. To discuss the amplitude and the phase of these waves, we rewrite the reflectivity in the form $r = r_0 + \delta r + (\delta r/2)(\eta + \eta^*)$, where $\eta \equiv \varepsilon e^{i(qx+\phi_{12})}$. The term $r_0 + \delta r$ is the coefficient for specular reflection, whereas $\delta r\eta$ and $\delta r\eta^*$ are proportional to the amplitudes for diffraction into the ± 1 diffraction orders. If we first consider probe P1, the two diffracted orders have wavevectors $\mathbf{k}_{P1} - \mathbf{q}$ and $\mathbf{k}_{P1} + \mathbf{q}$. Because the phase-matched geometry ensures that $\mathbf{k}_{P2} = \mathbf{k}_{P1} - \mathbf{q}$, the component of P1 whose wavevector is shifted by $-\mathbf{q}$ emerges collinear with the reflected wave from P2. This wave acquires the phase factor $\eta*$ as it diffracts from the transient grating. Turning next to probe P2, the diffracted wave whose wavevector is shifted by $+\mathbf{q}$ is diffracted into the path of P1. This wave acquires the conjugate phase factor η.

The absolute phase calibration is obtained by comparing the intensity of the beams that emerge from the sample along the directions defined by the specular reflections of P1 and P2. To see how this comes about, we write the amplitude of the incident probe beams in the phasor form $E_{P1,2} = E_P e^{i\phi_{P1,2}}$ (as the two beams propagate collinearly after interacting

with the sample we can ignore the spatial dependence of the phase). The amplitude in the specular path of P1 is $E_P[(r_0 + \delta r)e^{i\phi_{P1}} + (\delta r\eta/2)e^{i\phi_{P2}}]$ and the amplitude in the specular path of P2 is $E_P[(r_0 + \delta r)e^{i\phi_{P2}} + (\delta r\eta^*/2)e^{i\phi_{P1}}]$. The intensity, and therefore the photodetector current, for each of the two paths is proportional to the square of the phasor amplitude.

After neglecting terms that are second order in δr, we obtain $I_{P1,P2} = I_P^{eq} + \Delta I_{P1,P2}$, where I_P^{eq} is the dc value of the photo-detector current and proportional to the equilibrium reflectivity ($I_P^{eq} \propto |r_0|^2|E_P|^2$) independent of the pump beams . $\Delta I_{P1,P2}$ is the transient change in the photo-detector current induced by the pump beams. Expanding the equations above yields:

$$\frac{\Delta I_{P1}}{I_P^{eq}} = \left|\frac{\delta r}{r_0}\right| [cos(\phi_S) + (\varepsilon/2)cos(\psi - \phi_S)] \tag{5.2}$$

$$\frac{\Delta I_{P2}}{I_P^{eq}} = \left|\frac{\delta r}{r_0}\right| [cos(\phi_S) + (\varepsilon/2)cos(\psi + \phi_S)]. \tag{5.3}$$

To obtain $\Delta I_{P1,P2}$, we modulate the intensity of the pump beams and use a lockin amplifier to measure the change in $I_{P1,P2}$ at this frequency. Measuring the dc output of the photo-detector provides a direct measure of I_P^{eq}, and the ratio $\frac{\Delta I_{P1}}{I_P^{eq}}$ can readily be obtained experimentally.

In Eqs. 5.2 and 5.3, ϕ_S is the phase of δr with respect to r_0 and $\psi \equiv (\phi_{P1} - \phi_{P2}) - \phi_{12}$. Measuring ΔI_{P1} and ΔI_{P2} as a function of the phase angle ψ, together with I_P^{eq}, provides a complete characterization of the grating parameters, that is, $|\delta r/r_0|$, ε, and ϕ_S.

In Fig. 5.5, we show the experimental implementation of the heterodyne detection

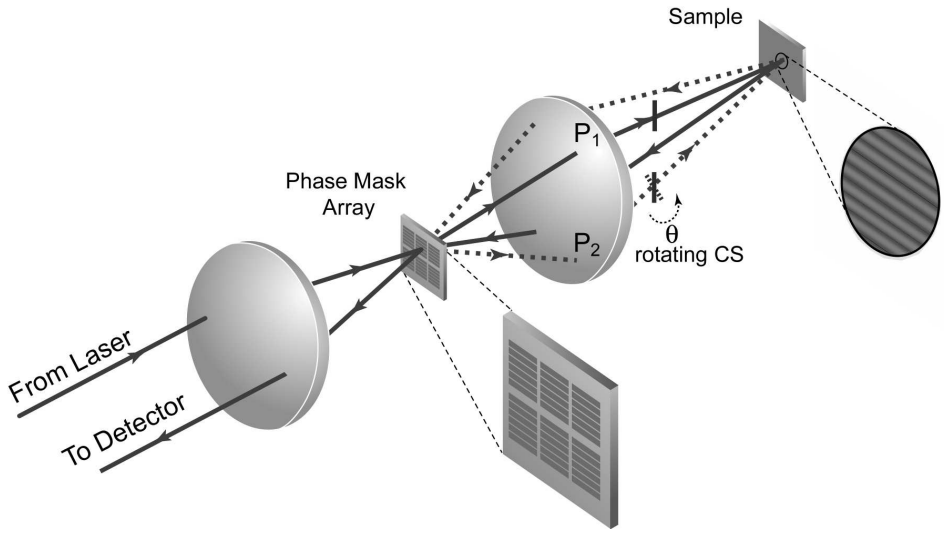

Figure 5.5: Experimental setup for measuring the absolute phase in transient grating experiments

and phase calibration (for clarity, only the probe beams are shown). A rotating coverslip is used to continuously change the phase difference, $\phi_{P1} - \phi_{P2}$, between the two probe beams. After reflection and diffraction from the surface of the sample, the probe beams pass through the same transmission grating in the reverse direction. They emerge from the grating with their collinearity restored and are sent to a photodetector.

The use of a diffractive optic beamsplitter makes it possible to measure the two currents, I_{P1} and I_{P2} without realignment of the setup. In performing the absolute phase calibration, we first block one of the reflected probes before it returns to the phase mask and allow the other reflected probe reach the detector. If P2 is blocked, for example, the detector current corresponds to I_{P1}. Measurement of I_{P2} requires only that we switch the beam stop to block the reflected P1.

By rotating one of the two coverslips placed in the probe beam paths, we can continuously change the phase ψ. If the angle of incidence of the probe on the coverslip

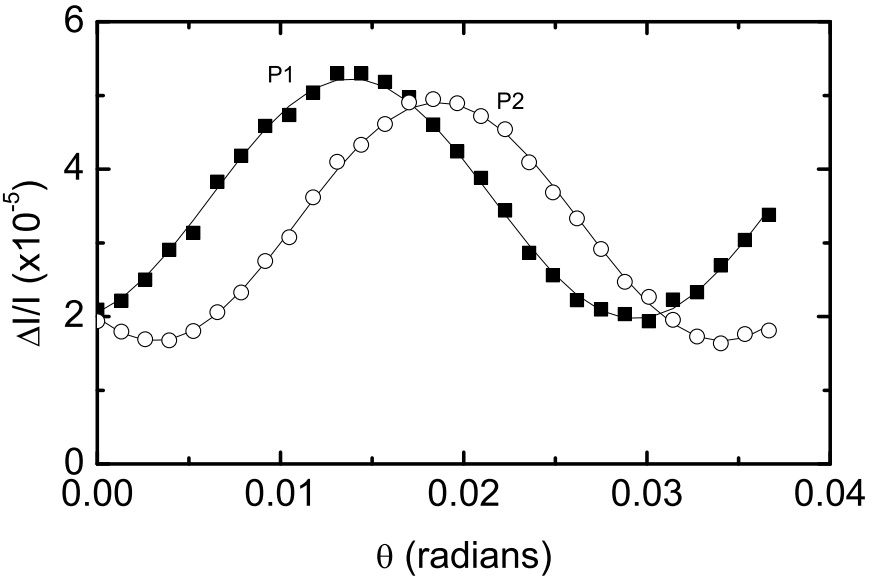

Figure 5.6: Fractional photoinduced change in intensity as a function of the cover slip angle (θ) in $Bi_2Sr_2CaCu_2O_{8+\delta}$. Solid lines are fits to Eqs. 5.4 and 5.5. The phase difference between the two cosines gives $2\phi_S = -0.96$ rad.

is close to 45^0, the change in ψ introduced by a small rotation is a linear function of the rotation angle, θ. Therefore, we can write $\psi(\theta) = k(\theta - \theta_0)$, where θ_0 and k are constants. In the setup, we mounted one of the coverslips on a rotational stepper motor which can change θ in steps of 0.001^0. Rotating this coverslip by approximately 2^0 changes the ψ by 2π.

To obtain ϕ_S, we record $\frac{\Delta I_{P1}(\theta)}{I_P^{eq}}$ and $\frac{\Delta I_{P2}(\theta)}{I_P^{eq}}$ as a function of θ. If we plug in the expression $\psi(\theta) = k(\theta - \theta_0)$ in to Eqs. 5.2 and 5.3, we get:

$$\frac{\Delta I_{P1}(\theta)}{I_P^{eq}} = \left|\frac{\delta r}{r_0}\right| [cos(\phi_S) + (\varepsilon/2)cos(k\theta - (k\theta_0 + \phi_S))] \tag{5.4}$$

$$\frac{\Delta I_{P2}(\theta)}{I_P^{eq}} = \left|\frac{\delta r}{r_0}\right| [cos(\phi_S) + (\varepsilon/2)cos(k\theta - (k\theta_0 - \phi_S))]. \tag{5.5}$$

Fig. 5.6 shows measurements of $\frac{\Delta I_{P1}(\theta)}{I_P^{eq}}$ and $\frac{\Delta I_{P2}(\theta)}{I_P^{eq}}$ on a high temperature super-

conductor ($Bi_2Sr_2CaCu_2O_{8+\delta}$) [16] at T= 5 K, measured near zero time delay between the pump and the probe. We fit these curves into the form $\frac{\Delta I_{P1,P2}(\theta)}{I_P^{eq}} = a + bcos(k\theta - \beta_{1,2})$ where a, b, k and $\beta_{1,2}$ are fit parameters. From the Eqs. 5.4 and 5.5, the values of a ($= \left|\frac{\delta r}{r_0}\right| cos\phi_S$), b ($= \left|\frac{\delta r}{r_0}\right| \varepsilon/2$) and k are going to be equal for P1 and P2. The values of β_1 ($= k\theta_0 + \phi_S$) and β_2 ($= k\theta_0 - \phi_S$) will be different for P1 and P2. From the obtained values of β_1, β_2 and k, we can get θ_0 and ϕ_S. After obtaining ϕ_S, from the values of a and b, we can get $\left|\frac{\delta r}{r_0}\right|$ and ε. Therefore, we have demonstrated a way of completely characterizing the photoinduced grating parameters $\left|\frac{\delta r}{r_0}\right|$, ε and ϕ_S. If we repeat this measurement at different pump probe delays, we will obtain these expressions as a function of time.

5.6 Data acquisition

In this section, we describe how we acquire data. In the actual experiment the first thing we do is to record the fractional change in the detector current as a function of the coverslip angle ($\frac{\Delta I_{P1,P2}(\theta)}{I_P^{eq}}$) for the two different probes. A typical plot is shown in Fig. 5.6. From the fits described in the previous section we obtain θ_0 and k. θ_0 is the position of coverslip for which the phase $\psi(\theta) = k(\theta - \theta_0)$ vanishes i.e. $\psi(\theta_0) = 0$. Since we know k we can calculate the positions of the coverslip (θ_1 and θ_2) for which $\psi(\theta_1) = \pi/2$ and $\psi(\theta_2) = \pi$.

Recording the $\frac{\Delta I_{P1,P2}(\theta)}{I_P^{eq}}$ for many different values of θ for both P1 and P2 is a time consuming process. Every time a control parameter (pump intensity, temperature etc...) is changed in the experiment, this needs to be repeated. Data taking can be simplified a lot by realizing that the values of k and θ_0 are independent of the sample properties. They

depend on the geometry of the setup itself. Once we obtain these values initially through the procedure described above, it is sufficient to record $\frac{\Delta I_P(\theta)}{I_P^{eq}}$ for only one of the probe beams and for the positions of the coverslip $\theta_i = \theta_0$, θ_1 and θ_2 for which $\psi(\theta_i) = 0$, $\pi/2$ and π. To see this, we plug in these values of ψ into Eq. 5.2, for$\psi = 0$

$$\frac{\Delta I_P(0)}{I_P^{eq}} = \left|\frac{\delta r}{r_0}\right| [cos(\phi_S) + (\varepsilon/2)cos(\phi_S)] \tag{5.6}$$

for $\psi = \pi/2$

$$\frac{\Delta I_P(\pi/2)}{I_P^{eq}} = \left|\frac{\delta r}{r_0}\right| [cos(\phi_S) + (\varepsilon/2)sin(\phi_S)] \tag{5.7}$$

and for $\psi = \pi$

$$\frac{\Delta I_P(\pi)}{I_P^{eq}} = \left|\frac{\delta r}{r_0}\right| [cos(\phi_S) - (\varepsilon/2)cos(\phi_S)] \tag{5.8}$$

This procedure gives three independent equations (Eqs. 5.6, 5.7 and 5.8) for three unknowns ($\left|\frac{\delta r}{r_0}\right|$, ε and ϕ_S). Recording these values as a function of time yields time dependent grating parameters.

Therefore, in practice when taking data we first follow the procedure in the previous section to obtain the values of k and θ_0. After this we only record $\frac{\Delta I_P(\theta)}{I_P^{eq}}$ for only one of the probe beams for three different positions of the coverslip. We have tested the stability of our system by measuring the phase drift after several hours. The phase shift was found to be less than $\Delta\psi = k\Delta\theta = 5^0$ out of 360^0 in three hours. This is another check on the validity of this method of data taking. From day to day, the position of the coverslip typically only changed by $\Delta\psi = k\Delta\theta = 15^0$. This also shows the extreme stability of our setup. We repeat the phase calibration if we change the grating wavelength or change the temperature by considerable amount since these might cause slight alignment changes.

In summary, we have described a diffractive optics based heterodyne detected transient grating setup in reflection geometry. We also discussed a new method of measuring the absolute phase of the photoinduced change in reflectivity in transient grating experiments. The phase is obtained by comparing the intensity of the two probe beams as a function of the phase change introduced by a rotating coverslip. This method resolves the long standing problem of calibration of the phase in transient grating experiments.

Chapter 6

Diffusion of Quasiparticles

6.1 Introduction

Quasiparticles are the elementary excitations of a superconductor, created when a Cooper pair of electrons breaks apart. The dynamic properties of quasiparticles, that is their rates of diffusion, scattering, trapping, and recombination, are critical for applications of conventional superconductors in X-ray detectors [3] and in the manipulation of superconductor-based qubits [34]. In more exotic superconductors, such as the high-T_c cuprates, a better understanding of quasiparticle dynamics may help to uncover the mechanism for Cooper pairing. A special property of the cuprate superconductors is the d-wave symmetry of the gap function, which leads to an unusual quasiparticle spectrum. The minimum energy for the creation of a quasiparticle depends on the direction of its momentum [47]. It is zero for momenta in the 'nodal' direction, oriented at 45° relative to the Cu-O bond. The most energetically expensive quasiparticles are the 'antinodal' ones, whose momenta are nearly parallel to the bond. The antinodal quasiparticles are the mystery particles

of cuprate superconductivity. Because they feel the pairing interaction most strongly, their properties may hold the key to high-T_c superconductivity. Unfortunately, their tendency to form strong pairs makes them difficult to study. In thermal equilibrium the population of quasiparticles is overwhelmingly dominated by the low energy nodal ones. As a result, transport measurements performed in equilibrium, such as microwave [26] and thermal [53] conductivity, are insensitive to antinodal quasiparticles.

6.2 Experimental methods

The details of the experimental technique is provided in Chapter 5. Here we only provide a brief summary. In this work a transient grating technique was developed and used to probe the transport of nonequilibrium quasiparticles in the high-T_c superconductor $YBa_2Cu_3O_{6.5}$. We find that the diffusion coefficient, D, is much smaller than the value obtained in measurements on equilibrium quasiparticles in the same material. The disparity in D suggests that the current experiment probes a population of quasiparticles that are not near the nodes, and are perhaps close to the antinodal regions of momentum space.

The nonequilibrium quasiparticles were introduced using short optical pulses. To probe their propagation, we generated a spatially periodic population by interfering two pulses at the sample surface. The spatial period, λ_g, equals $\lambda/2\sin\theta$, where λ is the wavelength of the pulse and 2θ is the angle between the two pump beams. The nonequilibrium quasiparticles cause a change in the index of refraction at the laser frequency [8] which is a linear function of their density [45]. As a result, the sinusoidal variation in quasiparticle density creates an index grating which can be detected by the diffraction of a probe pulse.

After creation, the distribution of quasiparticles evolves due to the combined effects of recombination and diffusion. In the process of recombination a pair of quasiparticles jumps back into the Cooper pair condensate with the simultaneous transfer of their creation energy to some other form (e.g. phonons). The amplitude of the grating may also decay as quasiparticle diffusion drives the system towards a spatially homogeneous quasiparticle concentration. The goal of the experiment is to disentangle these effects and measure both the rates of recombination and diffusion.

The transient grating technique has been used successfully in a wide variety of applications, including exciton diffusion, dynamics of biomolecules, propagation of ultrasound, and thermal diffusion [12]. Observing the propagation of superconducting quasiparticles requires the ability to detect the transient grating at extremely dilute concentrations. At the low excitation densities needed to detect their propagation, the quasiparticles produce no more than 10^{-5} fractional change in the index of refraction. The diffracted intensity from such a grating would therefore be of order 10^{-10} of the incident probe intensity and consequently very difficult to detect.

Detection of the grating required measurement of the amplitude of the diffracted wave, which is a part in 10^5 of the probe, rather than the intensity. This is accomplished through the use of heterodyne detection [51, 6]. The key element in the success of the heterodyne technique is the diffractive optic (DO) beamsplitter, which creates pairs of pump and probe beams [19, 38]. The DO element in our experimental setup (Fig. 6.1) is an array of 10 separate 2.5 mm square phase masks, each with a different grating period, on a fused silica substrate. A beam from a Ti:Sapphire laser (λ=800 nm and pulse repetition

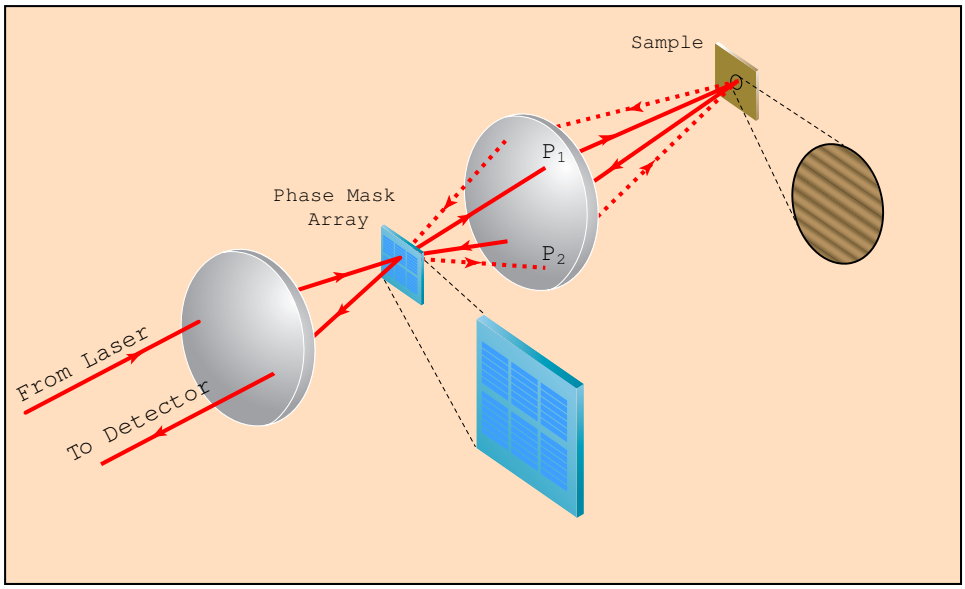

Figure 6.1: Illustration of the beam path for heterodyne transient grating detection. Pump and probe beams from the laser are split at the diffractive optic (for clarity only the probe beams are shown). A spherical mirror and plane folding mirror (represented schematically by a lens in the sketch) focus the beams to a single 100 μm spot on the sample. After specular reflection and diffraction at the sample surface, the two probe beams are recombined by the diffractive optic and directed to a Si photodiode detector. The wavevector of the quasiparticle density variation is changed, without optical realignment, by translating the diffractive optic so that a different phase mask in the array is inserted in the beam.

rate 80 MHz) is split into primary pump and probe beams, which are focused onto one of the phase masks at a small angle with respect to each other. The phase mask splits each of the primary beams by diffraction into the m=$\pm$1 orders. (For clarity, only the probe beam paths are shown in Fig. 6.1).

The interference of the two pump beams creates a spatially varying index of refraction in the sample which reaches a depth 1000 $\mathring{A}$ below the surface and has half the period of the phase mask. We detect the index variation using an implementation of the heterodyne technique that enables absolute calibration of the phase as explained in 5. Each of the two probe beams is specularly reflected from the surface of the sample, and returns,

via the DO, to a Si detector. The two possible round-trip beam paths are shown as solid and dashed lines in Fig. 6.1. With the use of the DO beamsplitter, detection of the diffracted probe is automatically aligned. The diffracted component of P1 is precisely collinear with reflected P2, and vice versa. The experiment is performed by alternately blocking one of the two reflected beams. If reflected P1 is blocked, then reflected P2 and diffracted P1 are mixed in the detector. This measurement by itself is insufficient to extract the wave amplitudes because the relative phase of P1 and P2 is undetermined. However, simply blocking reflected P2 instead of P1 produces a mixed signal with the conjugate phase. Comparing the detector output for the two conjugate beam paths fixes the absolute phase and therefore the wave amplitudes as well.

6.3 Experimental results

By adjusting the phase delay of P1 relative to P2, the output of the Si photodiode measures either the change of the specular reflection coefficient due to the grating, R, or the amplitude of the diffraction efficiency, TG. R is proportional to the spatial average of the quasiparticle concentration, whereas TG is proportional to the component of the quasiparticle concentration at the fundamental period of the grating, λ_g [15]. In Fig. 6.2 we plot both R and TG for λ_g =2 μm as a function of time delay, for several intensities of the excitation pulses, and consequently for a range of initial quasiparticle concentrations. The temperature of the sample was 5 K and the grating wavevector was oriented along the crystallographic **b** axis (parallel to the Cu-O chains).

The curves are normalized to their value at time delay zero. The R curves, which

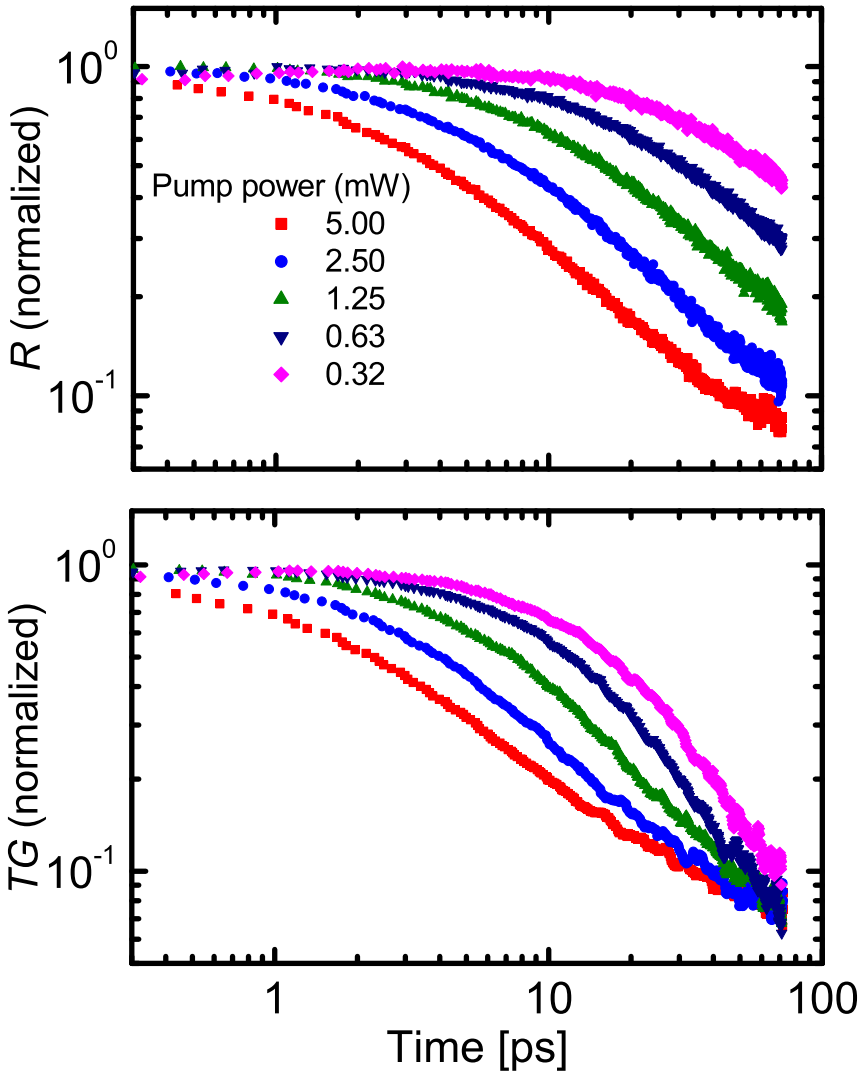

Figure 6.2: (top panel) Change in the specular reflection coefficient, R, as a function of time delay following creation of the grating, for several values of the pump intensity. R is normalized to unity at time delay zero to illustrate the systematic slowing down of the recombination rate as the excitation density is decreased. (bottom panel) Normalized amplitude of the diffracted probe beam as a function of time delay for the same values of pump intensity used to measure R.

decay due to recombination, are nonexponential, and their characteristic rate of decay increases with increasing concentration [45]. The increase of recombination rate with density is consistent with the idea that each quasiparticle must encounter another to scatter into the Cooper pair condensate. The corresponding TG curves depend strongly on the pump intensity as well. However the time dependence at each pump intensity is different from R because TG reflects the combined effects of recombination and propagation. In systems where the recombination rate is independent of density, it is relatively straightforward to separate the effects of particle decay and diffusion. If the average concentration decays exponentially with rate γ, the amplitude of the grating decays with rate $\gamma + Dq^2$, where D is the diffusion coefficient and q is the wavevector of the grating, $2\pi/\lambda_g$. The ratio TG/R, which decays simply as $\exp(-Dq^2t)$, isolates the effects of diffusion on the evolution of the particle density.

With this example in mind, we are led to consider TG/R for our data (see Fig. 6.3). The left, and right, panels show TG/R for grating periods of 2, and 5 μm, respectively, for several values of the pump laser intensity. Unlike the example of density-independent recombination, the decay of TG/R is nonexponential and highly dependent on the excitation density. At high intensity TG/R recovers its value at zero time delay, after an initial rapid decrease. TG/R is nearly independent of grating period at high intensity. As intensity decreases, the minimum of TG/R moves systematically towards longer times and the decay approaches a simple exponential. The exponential rate at low pump laser intensity clearly depends strongly on λ_g, as is expected if the grating decays due to diffusion.

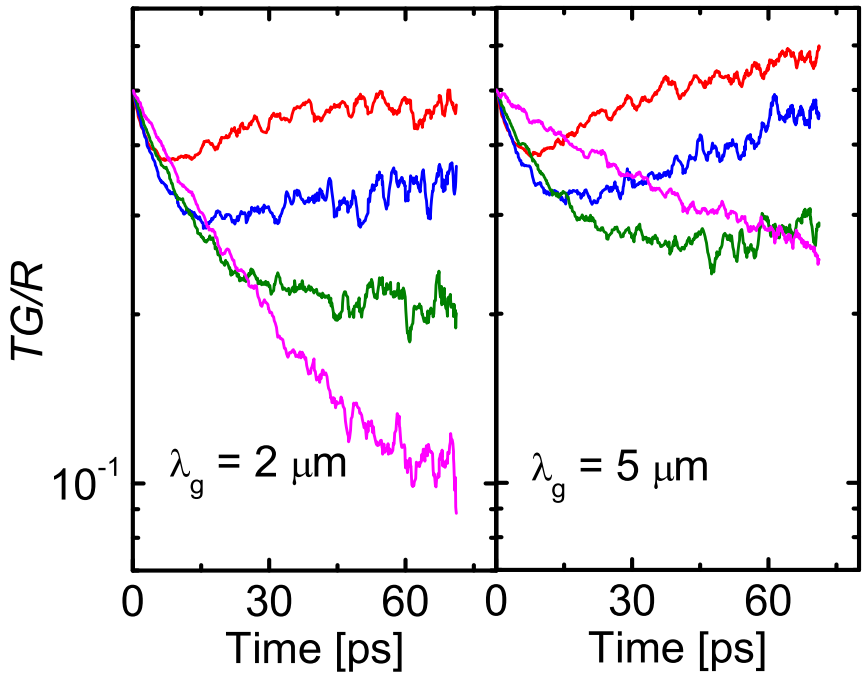

Figure 6.3: The ratio TG/R for the same pump intensities as in Fig. 6.2 (with P=0.63 mW omitted for clarity) for grating period 2μ (left panel) and 5μ (right panel). At high excitation density the curves are nearly independent of the period. At low excitation density the grating enters the propagation-dominated regime where the decay of TG/R depends strongly on the period of the grating.

6.4 Analysis of intensity dependence

The dependence of TG/R on laser intensity and grating period results from an interplay of density-dependent recombination, diffusion, and energy transfer. To unravel these effects we have modelled the quasiparticle dynamics by adding a quadratic recombination term to the diffusion equation: $\partial n(x,t)/\partial t = D\partial^2 n(x,t)/\partial x^2 - \beta n^2(x,t)$. Here, n is the quasiparticle density and β is the recombination coefficient, which is a measure of the inelastic scattering rate [43]. The dynamics predicted by this equation depend on the relative magnitude of βn and Dq^2. In the high density regime, $\beta n \gg Dq^2$, recombination

dominates over diffusion. Because the rate is more rapid where n is larger, recombination distorts the sinusoidal grating by flattening the crests. The distortion of the grating profile reduces the component of n at the fundamental grating period faster than its spatial average. This accounts for the initial decrease of TG/R. However, if this were the only process TG/R would never bounce back to its initial value, as it is seen to do in Fig. 6.3.

6.4.1 High intensity regime

TG/R recovers in the high-intensity regime because the energy released as the quasiparticles recombine appears in another form, one that also creates a change in the index of refraction. In conventional superconductors the quasiparticle energy is converted to lattice vibrational energy, which (in the presence of electron-phonon coupling) will change the index. While phonons may play this role in the cuprate superconductors as well, excitations involving the flipping of electron spins may be generated instead when quasiparticles recombine [43]. In either case, the recovery of TG/R follows if this secondary form of energy does not diffuse on the 100 ps time scale. In this case, the original sinusoidal distribution of energy is written into a stationary form of energy before the quasiparticles have had a chance to diffuse. When almost all the energy has been handed off from the quasiparticles to non-propagating modes, the grating recovers its sinusoidal profile and TG/R returns to its value at time zero. The energy remains frozen until the nanosecond time scale, when thermal diffusion becomes significant [37]. To illustrate this, we have numerically solved the diffusion equation given in previous section, the results are shown in Fig. 6.4.

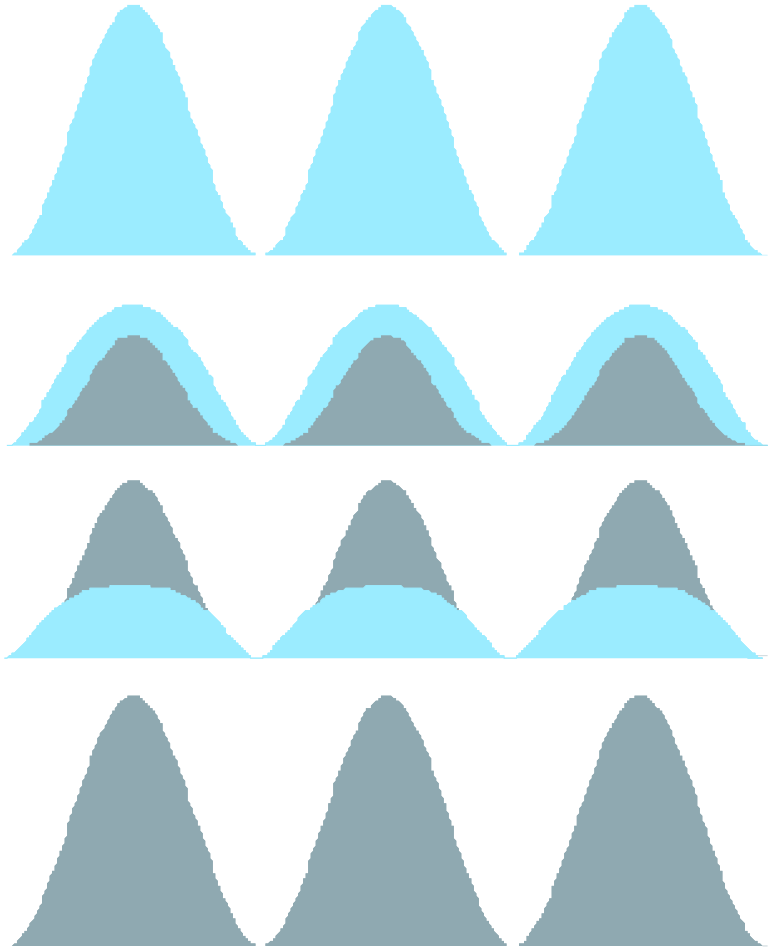

Figure 6.4: Evolution of the quasiparticle concentration ($n(x,t)$ which is shown in light-blue shading) in the recombination-dominated regime according to the equation given in the text. The pattern on the top is the initial density profile and the patterns below show its evolution in time. After creation, recombination is most rapid in the regions of highest quasiparticle density. The density-dependent recombination distorts the sinusoidal grating by flattening the crests. This leads to decay of TG/R even in the absence of diffusion. The grey regions show the energy accumulated as the quasiparticles recombine, which is proportional to $n(x,0) - n(x,t)$. The recovery of TG/R to its initial value at long times indicates that this energy is stored in non-propagating modes which also induce a change in the index of refraction. When all of the energy originally stored in the quasiparticles transfers to such modes, the index grating recovers its initial sinusoidal form, and TG/R approaches its value at time zero.

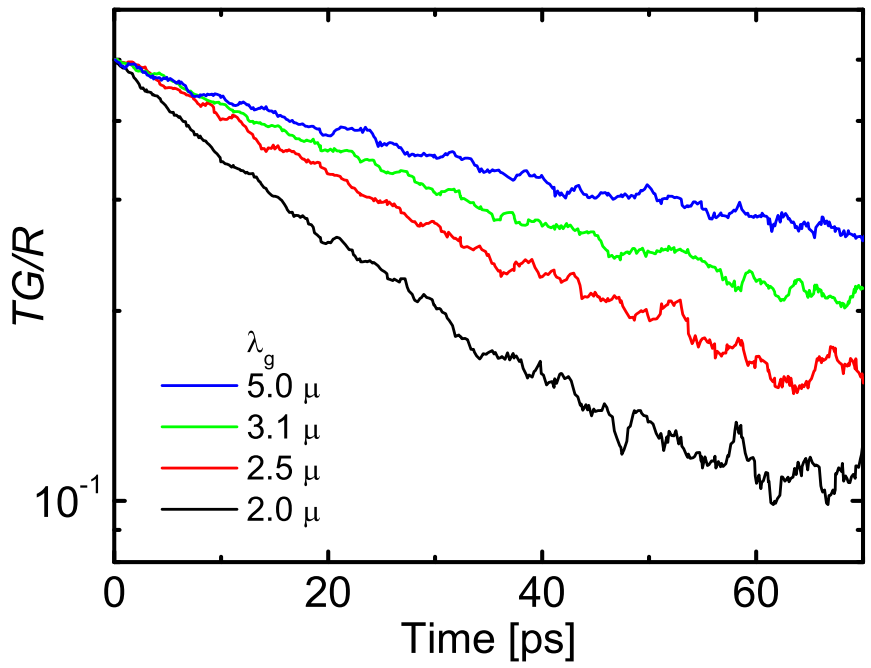

Figure 6.5: TG/R at low power (P=0.32 mW) for several grating periods between 2 and 5 μm. in underdoped YBCO at 5K

6.4.2 Low intensity regime

The effects of diffusion dominate in the low density regime, $\beta n \ll Dq^2$, where quasiparticle motion washes out the grating before energy transfer can take place. According to the equation governing $n(x,t)$, TG/R becomes q dependent and intensity independent in this limit. To find the rate of diffusion, we measured TG/R at low power (P=0.32 mW) for several grating periods between 2 and 5 μm shown in 6.5 . The initial decay rate of TG/R at low power is plotted as a function of q^2 in Fig. 6.6. The decay rate depends systematically on the grating period, demonstrating that the dynamics are in the propagation-dominated regime. The rates for the grating oriented along both the **a** and **b** crystallographic directions

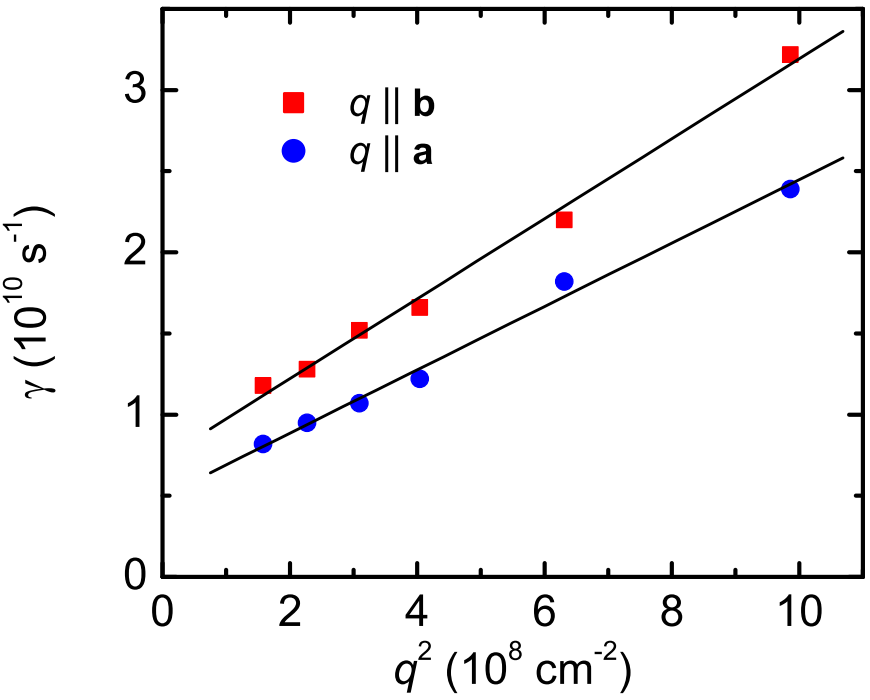

Figure 6.6: Initial decay rate of TG/R, for the same low intensity as in Fig. 6.3, plotted as a function of the square of the grating wavevector. Results are shown for two perpendicular orientations of the grating. The linear dependence of the rate on q^2 demonstrates that the propagation is diffusive. The slopes of linear fits yield diffusion coefficients $D_a = 20$ cm^2/s and $D_b = 24$ cm^2/s.

are plotted. For both directions the rate is a linear function of q^2, demonstrating that the quasiparticle propagation is diffusive. From the slope of a linear fit we determine that D_a=20 cm^2/s and D_b=24 cm^2/s. The intercept as q tends to zero is the decay rate due to recombination.

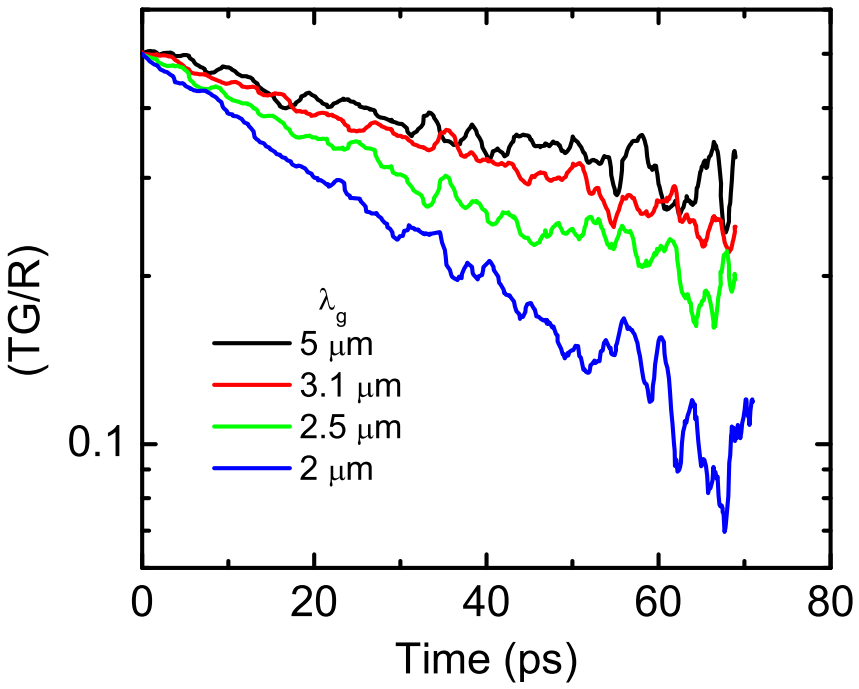

Figure 6.7: *TG/R* at low power (P=0.32 mW) for several grating periods between 2 and 5 μm. in underdoped BSCCO at 5K

6.5 Comparison with BSCCO

In the previous section, we presented measurements of diffusion constant in underdoped YBCO ($YBa_2Cu_3O_{6.5}$). It is of great interest to be able to compare YBCO with BSCCO. Optical experiments are capable of studying both samples contrary to scanning tunnelling microscopy (STM) and angle resolved photoemission spectroscopy (ARPES) which tend to work only for BSCCO. Recent STM experiments [33] show evidence of electronic inhomogeneity in 30 A^0 scale in BSSCO. But there are discussions whether observed inhomogeneity only exists at the surface or it is a property of bulk. Since the light at 820 nm penetrates about 100 unit cells, optically measured diffusion constant is a property of

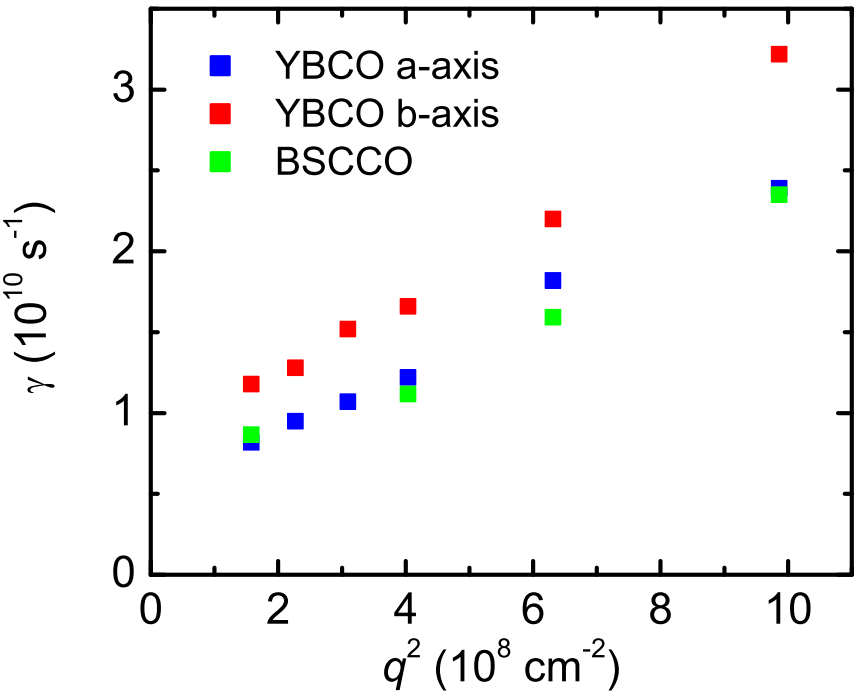

Figure 6.8: Initial decay rate of TG/R, for the same low intensity as in Fig. 6.3, plotted as a function of the square of the grating wavevector for both YBCO and BSCCO. Green points are for BSCCO and they lie on top of YBCO a axis data yielding a diffusion constant of $D = 20$ cm^2/s

bulk.

We have performed transient grating experiments in underdoped BSCCO single crystal with $T_c = 70$ K. These experiments are performed under the identical conditions to those described in Section 6.4.2. We studied the dependence of TG/R on the wave vector q of grating in BSCCO shown in Fig. 6.7. This is analogous to Fig. 6.5 in YBCO. Similar to Fig. 6.6 in YBCO, we can plot the initial decay rate of these curves as a function of q^2 of the grating. The results are shown in Fig. 6.8 as green points together with the YBCO data from Fig. 6.6. This plot shows that the diffusion in BSCCO is identical to diffusion

in YBCO along a axis. We will discuss the possible implications of this result in the next section.

6.6 Discussion

It is possible to infer the mean free time τ and mean square velocity $< v^2 >$ of nonequilibrium quasiparticles from the values of D quoted above. A lower bound on τ is obtained by inserting the maximum quasiparticle velocity, the Fermi velocity v_F, into the kinetic formula, $D =< v^2 > \tau/2$. The literature value [49] $v_F = 2 \times 10^7$ cm/s yields a lower bound of 100 fs. An upper bound on τ of essentially the same value can also be inferred from the experiment. If τ were significantly longer than 100 fs then quasiparticle propagation would be ballistic on the subpicosecond time scale. However, the time (see Fig. 6.9) and wavevector dependence of TG proves that quasiparticle motion is diffusive at the earliest times we can resolve, which is $\sim$ 300 fs after creation of the grating. Thus the allowed values of τ and v are narrowly bracketed near 100 fs and v_F, respectively. Furthermore, the measurements indicate that τ is determined by elastic, rather than inelastic, processes. The nonequilibrium particles survive for $\approx$ 100 ps, and therefore scatter $\approx$ 1000 times before decaying. This would be impossible if each scattering event resulted in a significant reduction of the quasiparticle's energy.

Equilibrium measurements find (in the same crystal and at the same temperature) that $\tau = 20$ ps [48], which is 200 times longer than τ of the nonequilibrium quasiparticles. The contrast suggests that the nonequilibrium quasiparticles are different from those present in thermal equilibrium. The equilibrium particles occupy states which have a small energy

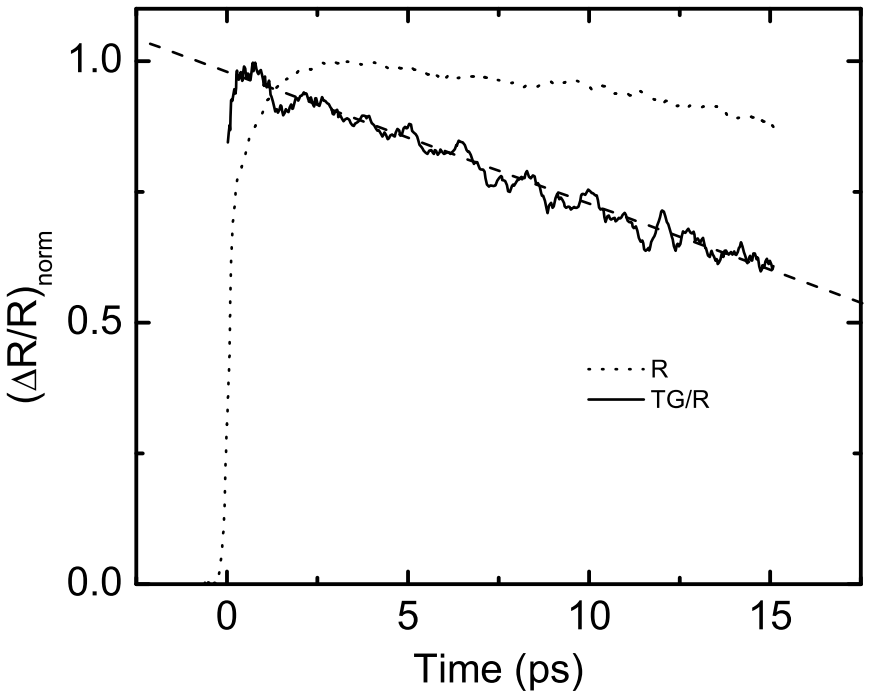

Figure 6.9: The mean value of the grating (R, shown as dotted line) and the ratio of the grating amplitude to the mean value (TG/R, shown as the solid line) at short times. The dashed curve shows that the ratio is exponential beginning at the earliest resolvable times, indicating that the diffusive motion is starts no later than the first 300 fs

(k_BT) relative to the chemical potential, and therefore lie very near the gap nodes. If the nonequilibrium quasiparticles are different, they must occupy higher energy states, perhaps ones closer to the antinodal regions of momentum space. It is possible that the constraints of momentum and energy conservation prevent relaxation of antinodal quasiparticles to the nodal regions. If the particles are antinodal, it is relevant to compare the width of the antinodal quasiparticle peak as measured by photoemission with $\hbar/\tau$ as measured by nonequilibrium transport. The peak width of 14 meV [14] corresponds to τ=50 fs, which is close to the transport value, particularly considering that photoemission is performed

on $Bi_2Sr_2CaCu_2O_8$ rather than $YBa_2Cu_3O_{6.5}$. The similarity of lifetimes suggests that the peak width in photoemission may be controlled by elastic scattering as well.

Finally, we discuss the implications of having identical diffusion coefficients in YBCO and BSCCO. As explained above, one can estimate a mean free time of 100 fs from the measured diffusion coefficient for both materials. If we convert this to a mean free path, we get a value of about 200 A^0. the significance of this number is that it is 5 to 6 times bigger than typical size of the patches seen in the STM experiment [33]. Unless the nonequilibrium quasiparticles are somehow not scattered by the boundaries of these patches, this would mean that the observed inhomogeneity lies in the surface rather than being in the bulk.

The transient grating method reported here promises to be broadly applicable to superconductors, as well as other materials in which there is a gap in the quasiparticle spectrum. The technique works readily in transmission or reflection geometry and therefore can be applied to bulk materials or thin films. The propagation of quasiparticles can be tracked in any system where nonequilibrium excitations generate a change in the index of refraction at the laser wavelength. In conventional superconductors, quasiparticle diffusion can be measured without fabricating trapping layers and junction detectors. In more exotic systems with multiple or anisotropic gaps, such as reported here, the transient grating technique can track the propagation of quasiparticles that conventional transport methods cannot detect.

Bibliography

[1] Y. Ando and K. Nakamura. Vortex phase transformations probed by the local ac response of $Bi_2Sr_2CaCu_2O_{8\ +\ delta}$ single crystals with various doping. *Physical Review B-Condensed Matter*, 59(18):R11661–4, 1999.

[2] R. D. Averitt, G. Rodriguez, A. I. Lobad, J. L. W. Siders, S. A. Trugman, and A. J. Taylor. Nonequilibrium superconductivity and quasiparticle dynamics in $YBa_2Cu_3O_{7\ -\ delta}$. *Physical Review B (Condensed Matter and Materials Physics)*, 63(14):140502–4, 2001.

[3] N. E. Booth and D. J. Goldie. Superconducting particle detectors. *Superconductor Science and Technology*, 9(7):493–516, 1996.

[4] S. D. Brorson, A. Kazeroonian, D. W. Face, T. K. Cheng, G. L. Doll, M. S. Dresselhaus, G. Dresselhaus, E. P. Ippen, T. Venkatesan, X. D. Wu, and A. Inam. Femtosecond thermomodulation study of high-T_c superconductors. *Solid State Communications*, 74(12):1305–8, 1990.

[5] Richard H. Bube. *Photoelectronic properties of semiconductors*. Cambridge University Press, Cambridge England ; New York, 1992.

[6] Y. J. Chang, P. Cong, and J. D. Simon. Optical heterodyne-detection of impulsive stimulated raman-scattering in liquids. *Journal of Physical Chemistry*, 99(20):7857–7859, 1995.

[7] May Chiao, R. W. Hill, Christian Lupien, Bojana Popic, Robert Gagnon, and Louis Taillefer. Quasiparticle transport in the vortex state of $YBa_2Cu_3O_{6.9}$. *Physical Review Letters*, 82(14):2943–2946, 1999.

[8] J. M. Chwalek, C. Uher, J. F. Whitaker, G. A. Mourou, and J. A. Agostinelli. Subpicosecond time-resolved studies of coherent phonon oscillations in thin-film $YBa_2Cu_3O_{6+x}$ (x-less-than-0.4). *Applied Physics Letters*, 58(9):980–982, 1991.

[9] J. Corson, J. Orenstein, Seongshik Oh, J. O'Donnell, and J. N. Eckstein. Nodal quasiparticle lifetime in the superconducting state of $Bi_2Sr_2CaCu_2O_{8\ +delta}$. *Physical Review Letters*, 85(12):2569–2572, 2000.

[10] J. Demsar, B. Podobnik, J. E. Evetts, G. A. Wagner, and D. Mihailovic. Evidence for crossover from a bose-einstein condensate to a bcs-like superconductor with doping

in $YBa_2Cu_3O_{7-\ delta}$ from quasiparticle relaxation dynamics experiments. *Europhysics Letters*, 45(3):381–6, 1999.

[11] G. L. Eesley, J. Heremans, M. S. Meyer, G. L. Doll, and S. H. Liou. Relaxation time of the order parameter in a high-temperature superconductor. *Physical Review Letters*, 65(27):3445–3448, 1990.

[12] H. J. Eichler, P. Gunter, and D. W. Pohl. *Laser-induced dynamic gratings*. Springer-Verlag, Berlin ; New York, 1986.

[13] M. Eschrig and M. R. Norman. Effect of the magnetic resonance on the electronic spectra of high-T_c superconductors. *Physical Review B (Condensed Matter and Materials Physics)*, 67(14):144503–23, 2003.

[14] A. V. Fedorov, T. Valla, P. D. Johnson, Q. Li, G. D. Gu, and N. Koshizuka. Temperature dependent photoemission studies of optimally doped $Bi_2Sr_2CaCu_2O_8$. *Physical Review Letters*, 82(10):2179–2182, 1999.

[15] I. M. Fishman, C. D. Marshall, J. S. Meth, and M. D. Fayer. Surface selectivity in 4-wave-mixing - transient gratings as a theoretical and experimental example. *Journal of the Optical Society of America B-Optical Physics*, 8(9):1880–1888, 1991.

[16] N. Gedik, J. Orenstein, Liang Ruixing, D. A. Bonn, and W. N. Hardy. Diffusion of nonequilibrium quasi-particles in a cuprate superconductor. *Science*, 300(5624):1410–12, 2003.

[17] N. Gedik, J. Orenstein, Liang Ruixing, D. A. Bonn, and W. N. Hardy. Gedik et al. reply. *Physical Review Letters*, 91(16):169702/1, 2003.

[18] G. D. Goodno, V. Astinov, and R. J. D. Miller. Diffractive optics-based heterodyne-detected grating spectroscopy: application to ultrafast protein dynamics. *Journal of Physical Chemistry B*, 103(4):603–7, 1999.

[19] G. D. Goodno, G. Dadusc, and R. J. D. Miller. Ultrafast heterodyne-detected transient-grating spectroscopy using diffractive optics. *Journal of the Optical Society of America B-Optical Physics*, 15(6):1791–4, 1998.

[20] K. E. Gray. Steady state measurements of the quasiparticle lifetime in superconducting aluminium. *Journal of Physics F: Metal Physics*, 1(3):290–308, 1971.

[21] Kenneth E. Gray and North Atlantic Treaty Organization. Scientific Affairs Division. *Nonequilibrium superconductivity, phonons, and Kapitza boundaries*. Plenum Press published in cooperation with NATO Scientific Affairs Division, New York, 1981.

[22] S. J. Hagen, Z. Z. Wang, and N. P. Ong. Anisotropy of the thermal conductivity of $YBa_2]Cu_3O_{7\ -\ y}$. *Physical Review B (Condensed Matter)*, 40(13):9389–9392, 1989.

[23] S. G. Han, Z. V. Vardeny, K. S. Wong, O. G. Symko, and G. Koren. Femtosecond optical detection of quasiparticle dynamics in high-T_c $YBa_2Cu_3O_{7\ -\ delta}$ superconducting thin films. *Physical Review Letters*, 65(21):2708–2711, 1990.

[24] W. N. Hardy, D. A. Bonn, D. C. Morgan, Ruixing Liang, and Kuan Zhang. Precision measurements of the temperature dependence of lambda in $YBa_2Cu_3O_{6.95}$: Strong evidence for nodes in the gap function. *Physical Review Letters*, 70(25):3999–4002, 1993.

[25] A. Honold, L. Schultheis, J. Kuhl, and C. W. Tu. Reflected degenerate four-wave mixing on GaAs single quantum wells. *Applied Physics Letters*, 52(25):2105–7, 1988.

[26] A. Hosseini, R. Harris, Saeid Kamal, P. Dosanjh, J. Preston, Ruixing Liang, W. N. Hardy, and D. A. Bonn. Microwave spectroscopy of thermally excited quasiparticles in $YBa_2Cu_3O_{6.99}$. *Physical Review B (Condensed Matter and Materials Physics)*, 60(2):1349–1359, 1999.

[27] P. C. Howell, A. Rosch, and P. J. Hirschfeld. Relaxation of hot quasiparticles in a d-wave superconductor. *Physical Review Letters*, 92(3):037003–4, 2004.

[28] J. Hwang, T. Timusk, A. V. Puchkov, N. L. Wang, G. D. Gu, C. C. Homes, J. J. Tu, and H. Eisaki. Marginal fermi liquid analysis of 300 k reflectance of $Bi_2Sr_2CaCu_2O_{8\ +\ \mathrm{delta}}$. *Physical Review B (Condensed Matter and Materials Physics)*, 69(9):094520–11, 2004.

[29] R. A. Kaindl, M. Woerner, T. Elsaesser, D. C. Smith, J. F. Ryan, G. A. Farnan, M. P. McCurry, and D. G. Walmsley. Ultrafast mid-infrared response of $YBa_2Cu_3O_{7-\ \mathrm{delta}}$. *Science*, 287(5452):470–3, 2000.

[30] S. B. Kaplan, C. C. Chi, D. N. Langenberg, J. J. Chang, S. Jafarey, and D. J. Scalapino. Quasiparticle and phonon lifetimes in superconductors. *Physical Review B (Solid State)*, 14(11):4854–4873, 1976.

[31] M. M. Kreitman. Low temperature thermal conductivity of several greases. *Review of Scientific Instruments*, 40(12):1562–5, 1969.

[32] M. M. Kreitman and J. T. Callahan. Thermal conductivity of apiezon n grease at liquid helium temperatures. *Cryogenics*, 10(2):155–9, 1970.

[33] K. M. Lang, V. Madhavan, J. E. Hoffman, E. W. Hudson, H. Elsaki, S. Uchida, and J. C. Davis. Imaging the granular structure of high-t/sub c/ superconductivity in underdoped $Bi_2Sr_2CaCu_2O_{8\ +\ \mathrm{delta}}$. *Nature*, 415(6870):412–16, 2002.

[34] K. M. Lang, S. Nam, J. Aumentado, C. Urbina, and J. M. Martinis. Banishing quasiparticles from josephson-junction qubits: why and how to do it. In *Applied Superconductivity Conference*, volume 13, pages 989–93, Houston, TX, USA., 2002. IEEE Transactions on Applied Superconductivity.

[35] Marc D. Levenson and Satoru Kano. *Introduction to nonlinear laser spectroscopy.* Academic Press, Boston, rev. edition, 1988.

[36] R. Liang, D. A. Bonn, and W. N. Hardy. Preparation and x-ray characterization of highly ordered ortho-ii phase $YBa_2Cu_3O_{6.50}$ single crystals. *Physica C*, 336(1-2):57–62, 2000.

[37] C. D. Marshall, I. M. Fishman, R. C. Dorfman, C. B. Eom, and M. D. Fayer. Thermal-diffusion, interfacial thermal barrier, and ultrasonic propagation in $YBa_2Cu_3O_{7-x}$ thin-films - surface-selective transient-grating experiments. *Physical Review B*, 45(17):10009–10021, 1992.

[38] A. A. Maznev, K. A. Nelson, and T. A. Rogers. Optical heterodyne detection of laser-induced gratings. *Optics Letters*, 23(16):1319–1321, 1998.

[39] H. J. A. Molegraaf, C. Presura, D. van der Marel, P. H. Kes, and M. Li. Superconductivity-induced transfer of in-plane spectral weight in $Bi_2Sr_2CaCu_2O_{8+delta}$. *Science*, 295(5563):2239–2241, 2002.

[40] M. R. Norman. Magnetic collective mode dispersion in high-temperature superconductors. *Physical Review B (Condensed Matter and Materials Physics)*, 63(9):092509–3, 2001.

[41] C. S. Owen and D. J. Scalapino. Superconducting state under the influence of external dynamic pair breaking. *Physical Review Letters*, 28(24):1559–61, 1972.

[42] W. H. Parker. Modified heating theory of nonequilibrium superconductors. *Physical Review B (Solid State)*, 12(9):3667–3672, 1975.

[43] S. M. Quinlan, D. J. Scalapino, and N. Bulut. Superconducting quasiparticle lifetimes due to spin-fluctuation scattering. *Physical Review B (Condensed Matter)*, 49(2):1470–1473, 1994.

[44] A. Rothwarf and B. N. Taylor. Measurement of recombination lifetimes in superconductors. *Physical Review Letters*, 19(1):27–30, 1967.

[45] G. P. Segre, N. Gedik, J. Orenstein, D. A. Bonn, Ruixing Liang, and W. N. Hardy. Photoinduced changes of reflectivity in single crystals of $YBa_2Cu_3O_{6.5}$ (ortho II). *Physical Review Letters*, 88(13):137001–4, 2002.

[46] Gino Paolo Segre. *Pump probe spectroscopy of quasiparticle dynamics in cuprate superconductors*. Phd, UNIVERSITY OF CALIFORNIA, BERKELEY, 2001.

[47] Z.-X. Shen, D. S. Dessau, B. O. Wells, D. M. King, W. E. Spicer, A. J. Arko, D. Marshall, L. W. Lombardo, A. Kapitulnik, P. Dickinson, S. Doniach, J. DiCarlo, T. Loeser, and C. H. Park. Anomalously large gap anisotropy in the a-b plane of $Bi_2Sr_2CaCu_2O_{8+delta}$. *Physical Review Letters*, 70(10):1553–1556, 1993.

[48] P. J. Turner, R. Harris, Saeid Kamal, M. E. Hayden, D. M. Broun, D. C. Morgan, A. Hosseini, P. Dosanjh, G. K. Mullins, J. S. Preston, Ruixing Liang, D. A. Bonn, and W. N. Hardy. Observation of weak-limit quasiparticle scattering via broadband microwave spectroscopy of a d-wave superconductor. *Physical Review Letters*, 90(23):237005–4, 2003.

[49] T. Valla, A. V. Fedorov, P. D. Johnson, Q. Li, G. D. Gu, and N. Koshizuka. Temperature dependent scattering rates at the fermi surface of optimally doped $Bi_2Sr_2CaCu_2O_{8+delta}$. *Physical Review Letters*, 85(4):828–831, 2000.

[50] C. M. Varma, P. B. Littlewood, S. Schmitt-Rink, E. Abrahams, and A. E. Ruckenstein. Phenomenology of the normal state of cu-o high-temperature superconductors. *Physical Review Letters*, 63(18):1996–1999, 1989.

[51] P. Vohringer and N. F. Scherer. Transient grating optical heterodyne detected impulsive stimulated raman-scattering in simple liquids. *Journal of Physical Chemistry*, 99(9):2684–2695, 1995.

[52] M. B. Walker and M. F. Smith. Quasiparticle-quasiparticle scattering in high-T_c superconductors. *Physical Review B (Condensed Matter and Materials Physics)*, 61(17):11285–11288, 2000.

[53] Y. Zhang, N. P. Ong, P. W. Anderson, D. A. Bonn, R. Liang, and W. N. Hardy. Giant enhancement of the thermal hall conductivity $kappa_{xy}$ in the superconductor $YBa_2Cu_3O_7$. *Physical Review Letters*, 86(5):890–893, 2001.